Apoptosis (2026) 31:91
https://doi.org/10.1007/s10495-026-02287-1

Spatially defined danger zone shapes gastric cancer progression through CCDC80$^+$ fibroblast–induced CD8$^+$ T cell dysfunction

Shaocong Mo[1] · Yulin Wang[2] · Rong Xiong[3] · Liqiu Ma[4] · Midie Xu[3] · Lei Wang[3] · Wenchao Gu[5]

Received: 26 November 2025 / Accepted: 18 January 2026 / Published online: 7 March 2026

Abstract

Gastric cancer (GC) shows marked heterogeneity driven by the tumor microenvironment, leading to therapeutic resistance and poor prognosis. Using spatial transcriptomics of invasive murine tumors and human GC samples, we identified a distinct stromal–immune–vascular core region, termed the 'danger zone', which is enriched in diffuse-type GC and strongly linked to advanced stage and an immunosuppressive tumor microenvironment. Non-negative matrix factorization using danger zone signature genes stratified GC patients into two subtypes, with Subtype 2 exhibiting worse survival and impaired immunotherapy response. An XGBoost classifier based on 13 key genes—including CCDC80, MSRB3, FBLN1, and SPARCL1—accurately predicted subtypes and prognosis across cohorts. Single-cell and spatial analyses identified CCDC80$^+$ fibroblasts as key drivers within the danger zone. Mechanistically, CCDC80$^+$ fibroblasts recruit effector CD8$^+$ T cells through CXCL12–CXCR4 signaling and induce their dysfunction by markedly upregulating PD-1 and TIM-3, thereby promoting exhaustion and apoptosis. The interactions were validated using fibroblast-CD8 + T cell co-cultures and CXCL12 blockade. Finally, a LightGBM model predicted danger zone scores directly from H&E slides, correlating with stromal infiltration and patient survival. This study defines the danger zone as a key spatial feature of GC progression and immunosuppression, offering novel biomarkers, prognostic tools, and therapeutic targets.

Keywords Gastric cancer · Spatial · Danger zone · CCDC80 · Fibroblasts · CXCL12

Shaocong Mo, Yulin Wang and Rong Xiong contributed equally to this work.

✉ Midie Xu
midiexu12@fudan.edu.cn

✉ Lei Wang
wanglei056713@163.com

✉ Wenchao Gu
sunferrero@gmail.com

[1] Department of Digestive Diseases, Huashan Hospital, Fudan University, Shanghai, China

[2] Department of Nephrology, Zhongshan Hospital, Fudan University, Shanghai, China

[3] Department of Pathology, Fudan University Shanghai Cancer Center, Shanghai 200032, China

[4] Department of Molecular Imaging and Theranostics, Institute for Quantum Medical Science, National Institutes for Quantum Science and Technology, Chiba, Japan

[5] Department of Artificial Intelligence Medicine, Graduate School of Medicine, Chiba University, Chiba 263-8522, Japan

Abbreviations

GC	Gastric Cancer
TME	Tumor Microenvironment
RCTD	Robust Cell Type Decomposition
MISTy	Multiview Intercellular Spatial modeling framework
NMF	Non-negative Matrix Factorization
LASSO	Least Absolute Shrinkage and Selection Operator
FFPE	Formalin-Fixed, Paraffin-Embedded
DMEM	Dulbecco's Modified Eagle Medium
FBS	Fetal Bovine Serum
qRT-PCR	Quantitative Reverse Transcription Polymerase Chain Reaction
ELISA	Enzyme-Linked Immunosorbent Assay
H&E	Hematoxylin and Eosin
GEO	Gene Expression Omnibus
PCA	Principal Component Analysis
UMAP	Uniform Manifold Approximation and Projection
ssGSEA	Single-Sample Gene Set Enrichment Analysis

GSVA	Gene Set Variation Analysis
GSEA	Gene Set Enrichment Analysis
MCP	Microenvironment Cell Populations
XGBoost	Extreme Gradient Boosting
CTRP	Cancer Therapeutics Response Portal
TIDE	Tumor Immune Dysfunction and Exclusion
CNV	Copy Number Variation
TCGA	The Cancer Genome Atlas
ACRG	Asian Cancer Research Group
ICI	Immune Checkpoint Inhibitor
TSA	Tyramide Signal Amplification
FAP	Fibroblast Activation Protein

Introduction

Gastric cancer (GC) is the second leading cause of cancer deaths worldwide [1]. Although numerous treatment options have been developed for gastric cancer, including surgical resection, adjuvant or preoperative radiotherapy, immunotherapy, and targeted therapy, patients exhibit heterogeneous responses and outcomes to these interventions [2–6]. Moreover, certain gastric cancer lesions exhibit high invasiveness and metastatic potential, contributing to poor patient prognosis [7, 8]. These clinical observations suggest significant heterogeneity among patients, which is largely driven by the composition, characteristics, and architecture of the tumor microenvironment (TME) [9].

With the development of single-cell and spatial omics, studies on the TME in GC have progressed from bulk-level profiling to spatio-temporal interaction analysis. Advances in single-cell technology have enabled increasingly comprehensive analysis of the highly heterogeneous cellular composition within the gastric cancer TME. Large-scale single-cell transcriptomic studies have identified key cell types in the GC TME [10–12], including INHBA–FAP-high fibroblasts, CCL2-expressing endothelial cells and fibroblasts, as well as functional alterations in immune cells. In contrast, spatial omics profiling of the GC TME remains in its early stages. Spatial metabolomics-based analyses of GC have revealed three tumor subtypes and three stromal subtypes with distinct metabolic profiles that may influence trastuzumab therapy efficacy [13]. Antibody-based spatial proteomics technologies have revealed how immune checkpoints are modulated in GC [14]. Previous studies have also combined spatial transcriptomics and spatial metabolomics in GC to uncover intratumoral metabolic heterogeneity and the spatial characteristics of immune-metabolic reprogramming [15]. However, spatial omics studies in gastric cancer lack integrated analysis with single-cell and spatial transcriptomics, limiting our understanding of the spatial cellular landscape.

In fact, there are already well-established paradigms for spatially analyzing cellular composition and interactions in other cancer types. For instance, spatial transcriptomics has revealed coordinated expression of TIGIT in exhausted T cells and its ligand NECTIN in pancreatic tumor cells [16]. In glioblastoma, IL-10 released from macrophages and microglia has been found to induce T-cell dysfunction [17]. Moreover, stromal-immune niches were found to modulate antitumor immunity in breast cancer. Tertiary lymphoid structures were also identified in renal cell carcinoma through spatial transcriptomics [18, 19]. Building on these studies, we aim to define the core regions of GC initiation and progression at the spatial transcriptomics level and explore the underlying mechanisms of cellular interactions. Furthermore, we are intrigued by how the spatial core regions of GC influence the heterogeneity of patient subtypes, given that the classifications proposed by The Cancer Genome Atlas (TCGA) and the Asian Cancer Research Group (ACRG) are based exclusively on bulk transcriptomics, which limits their ability to fully capture the complexity and heterogeneity of the gastric cancer TME [20, 21].

In this study, we identified a spatial "danger zone" closely associated with poor prognosis and the diffuse pathological subtype of GC, using both human and mouse GC spatial transcriptomics data. The danger zone score was found to correlate with a more immunosuppressive microenvironment and resistance to immune checkpoint inhibitors. The danger zone signature could stratify gastric cancer patients into two subtypes and, when combined with an XGBoost-based model, could predict prognosis across multiple cohorts. Mechanistically, we demonstrate that $CCDC80^{+}$ fibroblasts in the danger zone recruit effector $CD8^{+}$ T cells by upregulating CXCL12 expression, ultimately leading to their functional exhaustion. Our findings provide significant insights into the spatial core regions of GC and their impact on patient prognosis.

Materials and methods

Patients

Formalin-fixed, paraffin-embedded (FFPE) surgical specimens were obtained from patients with GC for this study. The study was approved by the Research Ethics Committee, and informed consent was obtained from all participants (Ethical code: 050432-4-2307E).

Cell culture and transfection

The murine fibroblast cell line NIH-3T3 (QuiCell, Shanghai, China) was cultured in Dulbecco's Modified Eagle Medium (DMEM; Gibco, Carlsbad, CA, USA) supplemented with 10% calf serum (Gibco), 100 U/mL penicillin, and 100 µg/mL streptomycin (Thermo Fisher Scientific, Waltham, MA, USA) at 37 °C in a 5% CO_2 humidified atmosphere. For transient transfection, NIH-3T3 cells were transfected with the pcDNA3.1-CMV-MCS-3xFLAG-hGH-polyA-EF1a-EGFP plasmid encoding murine Ccdc80 or an empty vector as control using Lipofectamine 2000 (Invitrogen, Carlsbad, CA, USA) according to the manufacturer's protocol. Transfection efficiency was preliminarily monitored via fluorescence microscopy for EGFP expression. Successful overexpression was confirmed via quantitative reverse transcription polymerase chain reaction (qRT-PCR) and Western blotting.

$CD8^+$ T cell isolation and activation

Primary $CD8^+$ T cells were isolated from spleens of 8-week-old C57BL/6 mice using a $CD8a^+$ T Cell Isolation Kit (Miltenyi Biotec, Bergisch Gladbach, Germany). Purified cells were cultured in RPMI 1640 medium (Gibco) containing 10% FBS, 1% penicillin-streptomycin, 1 × GlutaMAX (Gibco), 1 × Non-Essential Amino Acids (Gibco), 1 mM sodium pyruvate (Gibco), 10 mM HEPES (Gibco), and 50 µM β-mercaptoethanol (Sigma-Aldrich, St. Louis, MO, USA). Cells were activated with plate-bound anti-CD3 (5 µg/mL; BioLegend, San Diego, CA, USA) and soluble anti-CD28 (2 µg/mL; BioLegend) antibodies for 48 h in the presence of 50 U/mL recombinant murine IL-2 (PeproTech, Cranbury, NJ, USA).

Co-culture system

5×10^5 cells per mL activated $CD8^+$ T cells were co-cultured with NIH-3T3 fibroblasts transiently overexpressing CCDC80 or control fibroblasts at a 1:1 cell ratio in 12-well plates for 24 h. A CXCL12-blocking antibody (1 µg/mL; Biolegend) or isotype-matched control IgG (Biolegend) was added to the co-culture medium. $CD8^+$ T cell exhaustion level was measured via flow cytometry.

Reagents and antibodies

Western blot antibodies included anti-mouse CCDC80 (1:1000; Cat# PK90161S, Abmart, Shanghai, China), anti-β-Tubulin (1: 1000; Cat# 2146, Cell Signaling Technology), and HRP-conjugated goat anti-rabbit IgG (1: 2000; Cat# abs20002, Absin, Shanghai, China). Flow cytometry antibodies included anti-PD-1 (PE-conjugated; Cat# 135205, BioLegend), anti-TIM-3 (Alexa Fluor™ 488-conjugated; Cat# 53-5871-82, Invitrogen). Immunofluorescence antibodies included anti-fibroblast activation protein (FAP) (1:1000; Cat# ET1704-23, HUABIO, Hangzhou, China), anti-CCDC80 (1:100; Cat# HPA002266, Sigma-Aldrich), anti-CXCL12 (1:100; Cat# BS40377, BIOWORLD, Nanjing, China), and HRP-conjugated goat anti-rabbit IgG (H+L) (1:500; Cat# GB23303, Servicebio, Wuhan, China).

Enzyme-linked immunosorbent assay

The collected supernatant was assayed for CXCL12 using an ELISA kit (Cat# MCX120, R&D Systems, Minneapolis, MN, USA), following the manufacturer's instructions.

Immunofluorescence

FFPE gastric cancer tissue sections underwent standard deparaffinization, rehydration, and antigen retrieval. After permeabilization and blocking, sequential multiplex immunofluorescence was performed using the Tyramide Signal Amplification (TSA) system. Sections were incubated overnight at 4 °C with primary antibodies. Subsequently, sections were incubated with an HRP-conjugated secondary antibody for 1 h, followed by tyramide-fluorophore reagent. Antibody complexes were stripped by microwave treatment between cycles. After all targets were labeled, nuclei were counterstained with DAPI, and slides mounted with antifade medium. Imaging was performed using a fluorescence microscope.

Data acquisition and cohort enrollment

To identify spatial core regions by interrogating a highly invasive gastric cancer model, we employed a KRAS mutation combined with p53 loss (KP) gastric cancer model [22, 23]. Through a meta-search, we selected the spatially resolved transcriptomics dataset GSE186290 from the Gene Expression Omnibus (GEO) database [24]. This study performed spatial transcriptomic profiling of $KRAS^{G12V}$-expressing and p53-knockout GAstric Neoplasia (GAN-KP) organoids derived from GAN mice, which

exhibit greater invasive and metastatic potential [24, 25]. To enhance the generalizability beyond mouse spatial analyses, spatial transcriptomics data from human gastric cancer were additionally obtained from GSE251950 [26]. Only spatial transcriptomic sections from primary GC were included in the analysis. Spatial transcriptomics data of human colorectal cancer were downloaded from GSE225857. For the bulk transcriptomics cohorts of GC, we included a total of nearly 2,000 samples of GC patients, which were listed in Table 1 (Table 1). As many publicly available gastric cancer survival cohorts as possible were included. GSE63354 for Asia Cancer Research Group (ACRG) GC cohort, containing 300 patients with GC, was obtained from the GEO database. GSE84437 for South Korea cohort, GSE26253 for Samsung Medical Center (SMC) cohort, GSE15459 for Singapore Patient Cohort, GSE13861 for Yonsei University Severance Hospital cohort, GSE26899 for Korea University Guro Hospital (KUGH) cohort and GSE26901 for Kosin University College of Medicine (KUCM) cohort were also downloaded from the GEO database [27, 28]. Furthermore, transcriptomic data of Stomach Adenocarcinoma from TCGA (TCGA-STAD) were obtained from UCSC Xena and transformed into Transcripts Per Kilobase Million (TPM) format. Survival information and clinical traits of each dataset were also obtained. For ACRG, TCGA-STAD, GSE84437 and GSE15459, overall survival data were collected and analyzed. For GSE26253, recurrence-free survival data was obtained. For GSE13861, GSE26899 and GSE26901, data on both overall survival and recurrence-free survival were collected and analyzed. The median follow-up time and demographic characteristics of the enrolled patient cohort were recorded (Table S1, Table S2). For the ACRG database, the covariates considered included AJCC Stage (6th edition), Lauren subtype, ACRG subtype, and MSI status. The bulk RNA-seq expression profile of small bowel adenocarcinoma GSE61465 was downloaded for comparative analysis. Besides, single-cell RNA sequencing data of GSE167297 and GSE163558 were retrieved from the GEO database [12, 29]. Histological slide data for TCGA-STAD tumors were acquired from the TCGA database.

Table 1 Datasets used in the study

Datasets	Category	Sample used	Application
GSE186290	Spatial transcriptomics	Tumor ($n=1$)	Discovery
GSE251950	Spatial transcriptomics	Primary tumors ($n=9$)	Validation
GSE167297	scRNA-seq	Tumors ($n=6$)	Discovery
GSE163558	scRNA-seq	Primary tumor ($n=3$) Adjacent non-tumoral ($n=1$) Lymph node metastasis ($n=2$) Ovary metastasis ($n=1$) Peritoneum metastasis ($n=1$) Liver metastasis ($n=2$)	Validation
GSE63354	Bulk RNA profiles	Tumors ($n=300$)	Training
TCGA-STAD	Bulk RNA profiles	Tumors ($n=350$)	Validation
GSE84437	Bulk RNA profiles	Tumors ($n=433$)	Validation
GSE26253	Bulk RNA profiles	Tumors ($n=432$)	Validation
GSE15459	Bulk RNA profiles	Tumors ($n=192$)	Validation
GSE13861	Bulk RNA profiles	Tumors ($n=44$)	Validation
GSE26899	Bulk RNA profiles	Tumors ($n=74$)	Validation
GSE26901	Bulk RNA profiles	Tumors ($n=109$)	Validation

Spatially resolved transcriptomics data analysis

Spatial transcriptomics data processing

For spatially resolved transcriptomics, the Seurat pipeline (version 4.0.5) was applied to the spatial transcriptomic RNA-sequencing. Initially, low spots were filtered according to previous studies. The filtered data underwent normalization using the *SCTransform()* function on the "Spatial" assay. Principal component analysis (PCA) was performed using *RunPCA()* on the normalized data, retaining the first 30 dimensions for subsequent analyses. Nearest neighbors were identified with *FindNeighbors()*, and clustering was performed using *FindClusters()* to categorize the spots. Finally, UMAP dimensionality reduction was performed using RunUMAP() to visualize the spatial transcriptomic profiles. *SpatialDimPlot() and SpatialFeaturePlot()* were used to visualize the processed data.

Spatial feature genes extraction and scoring

The *FindAllMarkers() function* was used to identify feature genes of each Seurat cluster for spatially resolved transcriptomics. Only markers with a log fold change greater than 0.25 were included. A minimum expression threshold of 20% of cells per cluster was applied to filter the markers. *FindMarkers()* was used to identify feature genes which belonged to one cluster, with the log fold change threshold set to 0.5. Since the danger zone-specific spatial

marker genes were initially identified in a mouse model, we employed the convert_mouse_to_human_symbols() function from the nichenetr (version 1.1.0) package to map mouse gene symbols to their corresponding human orthologs, ensuring they could be validated in subsequent human samples [30]. The enrichment of the danger zone in human GC spatial transcriptomic samples was evaluated using the AddModuleScore() function from the Seurat package.

Spatial deconvolution and spatial co-localization analysis

Robust Cell Type Decomposition (RCTD) method of spacexr package (version 2.2.0) was used to integrate scRNA-seq data and spatial transcriptomics to conduct spatial deconvolution [31]. Doublet mode was set to full. For the spatial co-localization analysis, we employed two approaches: spatial neighborhood networks and MISTy [32, 33]. For spatial neighborhood network construction, the *kNN()* function from the dbscan package (version 1.1–12) was used to compute k-nearest neighbors based on the spatial coordinates, with the number of neighbors set to 6. Next, the network was filtered by distance and rank to select relevant neighbors, creating the spatial neighborhood network. Finally, the start and end points of the network were combined with their spatial coordinates for subsequent visualization. Spatial co-localization of cell types was further analyzed using the mistyR package (version 1.0.3), which included three spatial views: intraview (assessing co-localization within a spot), the juxtaview (focusing on nearby cells with a distance of 5 spots), and the paraview (examining broader spatial relationships with a distance of 15 spots). Additionally, the SPOTlight package (version 1.5.2) was used to generate correlation matrices of the deconvolution result, enabling a comprehensive evaluation of spatial interactions among cell types [34].

Developmental trajectory analysis and spatial communication analysis

Monocle2 (version 2.22.0) and stlearn (version 0.4.0) were used for spatial trajectory analysis [35, 36]. For Monocle2, a CellDataSet object was initially created. Size factors were estimated using the *estimateSizeFactors()* function, followed by the calculation of gene dispersion with *estimateDispersions()* to assess variability across cells. Differential expression analysis was then conducted and Differential expressed genes were filtered and set as ordering genes using *setOrderingFilter()*. The dimensionality of the dataset was reduced and cells were ordered along the inferred trajectory using *orderCells()*. Importantly, the pseudotime values were incorporated into the spatial Seurat object and were visualized using *SpatialFeaturePlot()* to reveal the spatial developmental trajectory. For stlearn, we segmented the image into 40-pixel tiles with *st.pp.tiling()*. High-level features were then extracted from each tile using a deep learning model with *st.pp.extract_feature()*, enhancing spatial information for downstream analysis. Pseudotime was calculated for spatial spots based on the PCA-reduced data and cluster labels ("louvain") *using st.spatial.trajectory.pseudotime()*, with an epsilon parameter of 50. We further mapped global pseudotime trajectories between clusters using *st.spatial.trajectory.pseudotimespace_global()*.

Spatial communication analysis

Spatial communication analysis was performed using the COMMOT package (version 0.0.3) and CellChat package (version 1.1.3) [37, 38]. For COMMOT analysis, the ligand-receptor interaction database from CellChat was utilized. The *spatial_communication()* function was used to calculate sender and receiver signals. Communication directionality and patterns were assessed with the *communication_direction()* function. For spatial CellChat analysis, a CellChat object was created using the createCellChat() function, specifying the datatype as "spatial", along with spatial coordinates and corresponding scale factors. Ligand-receptor pairs in CellChatDB.human database were utilized. Overexpressed genes and ligand-receptor pairs were identified through the *identifyOverExpressedGenes()* and *identifyOverExpressedInteractions()* functions. Additionally, we visualized a specific signaling network using *netVisual_aggregate()* with a spatial layout.

Single cell data analysis

Single cell RNA sequencing data processing

For scRNA-seq data, the standard Seurat pipeline was applied. The PercentageFeatureSet() function was used to determine the mitochondrial gene percentage and hemoglobin gene expression percentage. Cells were filtered to retain high-quality cells, defined as those expressing between 200 and 2500 genes, with less than 20% mitochondrial gene content and less than 3% hemoglobin gene expression. Data normalization was performed using the *NormalizeData()* function with the "LogNormalize" method and a scale factor of 10,000. Highly variable genes were identified using the *FindVariableFeatures()* function with the "vst" method. The dataset was scaled using *ScaleData()*, and principal component analysis (PCA) was conducted with *RunPCA()*. Cell clustering was performed by first constructing nearest-neighbor graphs using the FindNeighbors() function, followed by applying the Louvain algorithm via FindClusters()

to delineate distinct cellular subpopulations. These clusters were subsequently projected into a low-dimensional space using UMAP for visualization. The processed single-cell RNA-seq dataset was further subjected to cell-type identification and annotation. Marker genes for epithelial, immune, and stromal cell types were selected based on established literature.

Single-cell gene set scoring, differential expression analysis and cell-cell communication

The *AddModuleScore()* function was applied for gene set scoring. Differential expression analysis between gene-positive and gene-negative clusters was performed using the *FindAllMarkers()* and *FindMarkers()* functions. Additionally, marker genes of the cell subpopulations were extracted from the differential expression analysis. Cell–cell interactions were evaluated using the CellChat package (version 1.1.3) [38]. Similar to the spatial CellChat analysis, the probability of communication between cell types was calculated, and signaling pathways were inferred. Only cell groups containing at least ten cells were retained for analysis. The resulting cell-cell communications were aggregated, and the interaction network was visualized using bubble plots. Additionally, the aggregated network of specific signaling pathways was visualized to highlight the underlying communication dynamics.

Transcription factor analysis

The pySCENIC workflow was performed following the standard three-step procedure [39]. First, single-cell gene expression data were preprocessed and converted into a loom file. Gene regulatory network inference was conducted with pyscenic grn using the GRNBoost2 method. The identified regulons were then refined with pyscenic ctx, integrating motif enrichment and cis-regulatory information from the cistarget databases. Finally, regulon activity scores at the single-cell level were quantified by pyscenic aucell, producing a regulon activity matrix stored in the output loom file. Downstream visualization and cell type–specific regulon analysis were performed in R, with functions such as *get_regulons()*, *get_regulons_AUC()*, and *calcRSS()* to identify and display cell type–specific transcription factors and their activity patterns.

Gene set enrichment analysis, functional enrichment and immune cell infiltration evaluation

Single-sample gene set enrichment analysis (ssGSEA) was applied to the bulk RNA-seq data using gene sets defined from spatially resolved transcriptomics, implemented via the GSVA package (version 1.38.2) [40]. Gene Ontology enrichment and gene set enrichment analysis (GSEA) were performed using the clusterProfiler package (version 4.2.2) [41]. The ESTIMATE algorithm was used to calculate immune and stromal scores, using the estimate package (version 1.0.13) [42]. MCP-counter (version 1.2.0) was used to evaluate immune cell infiltration, including T cells, B lineage, NK cells, and the monocytic lineage [43].

Subtyping and machine learning

The Non-negative Matrix Factorization (NMF) method was applied to the matrix for subtyping, using the "brunet" method with 100 iterations. The optimal rank was selected based on the point where the cophenetic coefficient began to decrease sharply. For machine learning, feature genes were first selected. Specifically, the *extractFeatures()* function from the NMF package (version 0.23.0) was used to extract genes highly ranked in determining NMF subtypes. These genes were further processed using Boruta random forest (maxRuns = 100, ntree = 500) and 10-fold cross-validated Least Absolute Shrinkage and Selection Operator (LASSO) [44]. We then employed seven machine learning algorithms for ensemble learning, including Naïve Bayes, Logistic Regression, Classification Tree, Random Forest, AdaBoost, XGBoost, and LightGBM. For Naïve Bayes, Classification Tree, Random Forest and AdaBoost, dichotomous discriminated results were output [45]. For Logistic Regression, XGBoost, and LightGBM, probabilistic outputs were generated. In both the training and validation sets, patients with predicted probabilities greater than 0.5 were classified as Subtype 2, and those with probabilities less than 0.5 were classified as Subtype 1. Accuracy, sensitivity, specificity, precision, F1 score, and Matthews Correlation Coefficient (MCC) were used to evaluate model performance. SHapley Additive exPlanations (SHAP) was used to interpret the contribution of each variable in the model to each sample, with SHAPforxgboost package (version 0.1.1).

Chemotherapy drugs and immune checkpoint inhibitor therapy sensitivity prediction

Drug sensitivity data and gene expression profiles of human cell lines were obtained from the Cancer Therapeutics Response Portal (CTRP). The pRRophetic package (version 0.5) was used to predict drug sensitivities for the ACRG cohort by integrating bulk gene expression profiles, cell line expression data, and drug sensitivity information [46]. For each drug, a lower area under the curve (AUC) indicated higher sensitivity. We utilized ridge regression via the calcPhenotype() function to model drug sensitivity. For each compound, the mean predicted AUC values were calculated

for both Subtype 1 and Subtype 2, followed by computation of the log2-transformed fold change. Compounds with a log2 fold change greater than 0.2 or less than − 0.2 were considered significant and selected. Moreover, the Tumor Immune Dysfunction and Exclusion (TIDE) web tool (tide.dfci.harvard.edu) was used to predict responses to immune checkpoint inhibitor (ICI) therapy, using centralized expression data as input [47]. To validate the impact on ICB response in a real-world setting, gene expression and clinical data from the IMvigor210 cohort were extracted using the IMvigor210CoreBiologies package (version 1.0.0). Although this cohort comprises patients with urothelial carcinoma, its rich clinical annotations provide valuable insights into the association between the danger zone score and response to ICIs. GSVA scores were further correlated with real-world ICI treatment responses.

Pathological image data acquisition, segmentation, feature extraction, and score prediction model

High-resolution digital pathology slides were read using the OpenSlide library and systematically processed with core modules from the Histolab library. Low-quality samples lacking metadata required to determine magnification levels were excluded. The entire slide was partitioned using the GridTiler strategy with the following parameters: tile size of 224 × 224 pixels, a tissue coverage threshold of ≥ 25%, zero overlap between tiles (pixel_overlap = 0), with segmentation performed at level 1.

High-level features were extracted from image tiles using a pretrained convolutional neural network. Specifically, the ResNet-50 model pretrained on the ImageNet dataset was employed [48]. Image tiles were read with OpenCV, converted to RGB format, normalized in size, transformed into tensors, and channel-wise standardized (parameters: mean=[0.485, 0.456, 0.406], std=[0.229, 0.224, 0.225]). Feature maps were obtained by forwarding the tiles through the network and capturing the output from the "layer4" layer. A global max pooling operation across spatial dimensions was applied to compress each channel's activation map into a single maximum value, resulting in a 2048-dimensional feature vector.

Based on the extracted pathology features, a danger zone score prediction model was constructed. The feature matrix was standardized using Z-score normalization via StandardScaler. Patients were randomly split into a 70% training set and a 30% validation set. The danger zone score for each TCGA patient was calculated using ssGSEA as the predicted outcome. Due to the large number of tiles, a LightGBM regression framework was employed to accelerate computation and construct the prediction model. The predictions from all tiles belonging to the same patient were averaged to generate a patient-level danger zone score. Model performance was evaluated using patient-level metrics including the coefficient of determination (R^2), root mean square error (RMSE), Pearson correlation coefficient, and Spearman rank correlation coefficient. Finally, prediction scores of image tiles were mapped back onto the corresponding pathology slides using their spatial information, enabling visual interpretation of the relationship between pathological regions and model-generated scores.

Genomic analysis

Copy number variation (CNV) data of TCGA-STAD were obtained from the Xena UCSC. CNV values greater than 0 were considered GAIN variants, while values less than 0 were considered LOSS variants. The copy number alterations of key genes were further investigated. Somatic mutation data were downloaded from GDC TCGA (https://gdc.cancer.gov/). The maftools R package was used to analyze and visualize somatic mutations between subtypes [49]. Mutation frequencies and patterns were visualized using *oncoplot()* function to display the top 30 mutated genes. For protein sequence variations, *lollipopPlot()* was utilized to visualize mutations in genes of interest such as TP53. To characterize mutational signatures, trinucleotide contexts were derived using the *trinucleotideMatrix()* function with the hg38 human reference genome. Non-negative matrix factorization (NMF) was subsequently employed through *estimateSignatures()* to determine the optimal number of mutational signatures. These signatures were then benchmarked against the COSMIC reference database by computing cosine similarity. Additionally, genomic microsatellite instability statuses for TCGA-STAD samples were sourced from The Cancer Immunome Atlas (https://tcia.at/).

Statistical analysis

Continuous variables between two groups were compared using the Wilcoxon rank-sum test. For comparisons among three or more groups, the Kruskal–Wallis test was used. Categorical variables were compared between two groups using the chi-square test. Univariate Cox regression analysis was performed to identify prognostic factors using the survival package. Kaplan–Meier analysis was applied to evaluate clinical outcomes, and statistical significance was determined using the log-rank test. The surv_cutpoint function in the survminer package was used to determine the optimal cutoff. Correlations were assessed using Spearman's rank correlation coefficient. All statistical analyses were conducted using R (version 4.1.3) and Python (version 3.9.11).

Results

Spatial transcriptomics identified a stromal, vascular and immune core region of invasive GC

The workflow of the study was shown in Fig. 1a (Fig. 1a). To explore the crucial zones of invasive GC based on spatial dissection, we employed the spatial transcriptomic sequencing data of GAN-KP tumor of mice, an experimental model of highly invasive and metastatic gastric tumor. Twelve clusters were identified through dimensionality reduction and mapped in the transcriptomic slide (Fig. 1b). Based on key marker genes, it was striking to notice that markers of immune cells (Ptprc), stromal cells (Pecam1, Acta2 and Vwf) were consistently highly expressed in Cluster 3, which was spatially located between Cluster 1 and Cluster 4 (Fig. 1c, Fig. S1a). Density plots using Nebulosa package also underscored the remarkable enrichment of immune and stromal gene expression in Cluster 3 (Fig. 1d).

To directly elucidate the influence of distinct spatial clusters on the survival outcomes of GC patients, we proceeded to identify the marker genes for each cluster and converted them into their human homologs. In the ACRG GC cohort, we applied the ssGSEA method to quantify the scores of each spatial transcriptomic cluster, followed by univariate Cox regression analysis to evaluate the impact of these cluster scores on patient survival. Cluster 3, Cluster 1, and Cluster 4 were significantly associated with poorer prognosis, with Cluster 3 exhibiting the most pronounced detrimental effect (Fig. 1e). We then applied pseudotime analysis of Cluster 3, Cluster 1 and Cluster 4, which further revealed that Cluster 3 could be an intermediate state in the transition from Cluster 1 to Cluster 4 (Fig. 1f). To gain an initial insight into the function of Cluster 3, we then performed GO enrichment analysis on its marker genes, which revealed

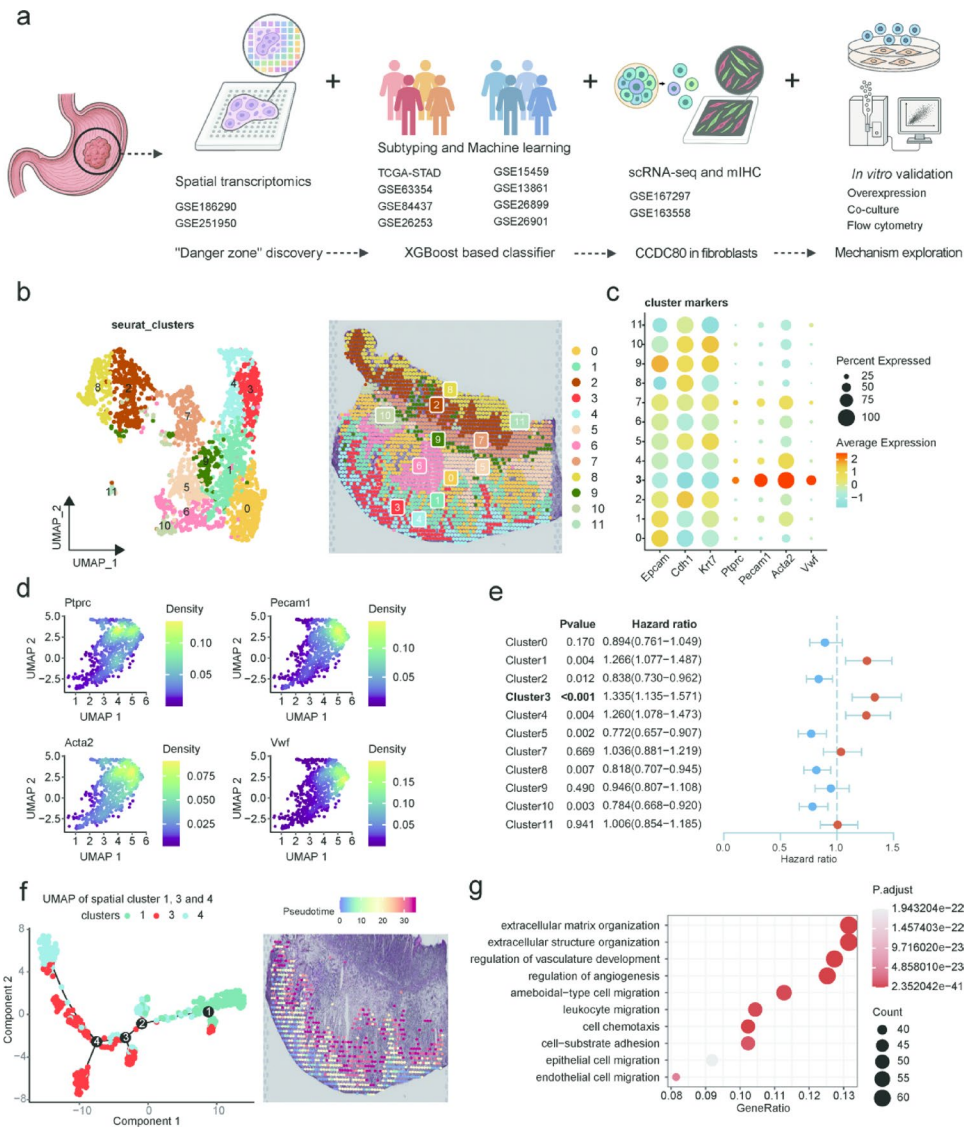

Fig. 1 Spatial transcriptomics identifies a stromal-vascular-immune core driving invasion and poor prognosis in gastric cancer. **a** Workflow of the study. **b** Twelve transcriptomic clusters mapped onto a spatial slide after dimensionality reduction. **c** Spatial co-expression of immune (Ptprc) and stromal (Pecam1, Acta2, Vwf) markers in Cluster 3. **d** Nebulosa density plots confirming enrichment of immune/stromal genes in Cluster 3. **e** Univariate Cox regression of human-homolog cluster scores (ACRG cohort), showing that Clusters 1, 3, and 4 are associated with poor survival, with Cluster 3 showing the strongest association. **f** Pseudotime trajectory analysis positioning Cluster 3 as an intermediate state between Clusters 1 and 4. **g** GO enrichment of Cluster 3 marker genes highlighting extracellular matrix, angiogenesis, and immune pathways

significant enrichment in pathways related to extracellular matrix organization, angiogenesis, and immune responses (Fig. 1g). In conclusion, Cluster 3, located near the serosal layer in the spatial landscape of gastric cancer, is characterized by prominent immune and stromal aggregation and might be associated with unfavorable survival outcomes.

Human spatial transcriptomics and pathology reveal cluster 3 as a spatial "danger zone" shaping the TME

To further elucidate the relationship between the aforementioned Cluster 3 and the pathological characteristics of GC, we compared Cluster 3 scores across different clinical features in the ACRG cohort. We observed a clear upward trend of Cluster 3 score with increasing AJCC stages (Fig. 2a). Notably, Cluster 3 genes exhibited significantly elevated expression in the MSS/EMT subtype of the ACRG molecular classification (Fig. 2b). This subtype has been well-documented as predominantly presenting at advanced stages, with a high recurrence rate, increased peritoneal dissemination, and the poorest prognosis. Interestingly, Cluster 3 signature genes also scored significantly higher in the diffuse type of the Lauren classification, which is widely recognized as a subtype with poor prognosis (Fig. 2c). These findings suggest that the immune-stroma-enriched key region identified from GAN-KP murine GC was indeed closely associated with adverse molecular pathological

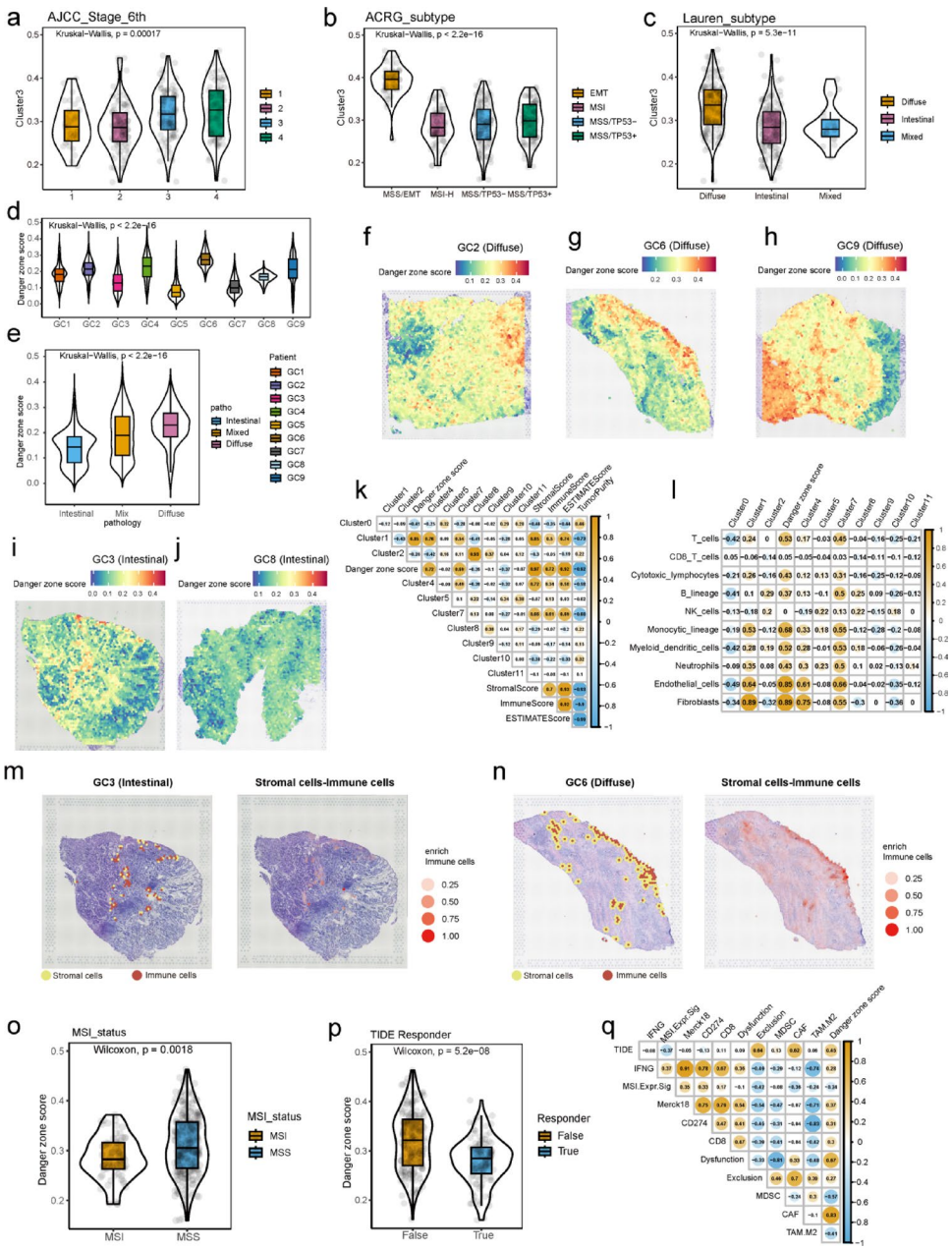

Fig. 2 Spatial danger zone identified in human gastric cancer drives immunosuppressive TME. **a** Quantification of Cluster 3 scores across AJCC stages in the ACRG cohort. **b** Quantification of Cluster 3 scores across MSS/EMT molecular subtypes in the ACRG classification. **c** Comparison of Cluster 3 scores between diffuse-type and intestinal-type tumors in the Lauren classification. **d** Danger zone scores across all human spatial transcriptomic samples. **e** Danger zone scores across stratified by Lauren subtypes (diffuse/mixed vs. intestinal). **f-h** Definition of high-scoring danger zone regions in diffuse-type samples GC2 **f**, GC6 **g**, and GC9 **h**. **i**, **j** Spatial mapping of danger zone scores in intestinal-type samples GC3 **i** and GC8 **j**. **k** Correlation analysis of spatial cluster scores with stromal, immune, and ESTIMATE scores. **l** MCP-counter reveals danger zone's association with fibroblasts, endothelial cells, and immune infiltration. **m-n** Spatial neighborhood network analysis in human spatial transcriptomes of diffuse-type **m** and intestinal-type **n** patients. **o** Danger zone scores in MSS and MSI tumors in ACRG cohort. **p** Danger zone scores in non-responders and responders to ICIs predicted by TIDE algorithm. **q** Correlation of danger zone score with signatures of TIDE

phenotypes in human GC. Therefore, we named Cluster 3 the spatial "danger zone". To further substantiate the existence of the danger zone in human GC and its association with molecular pathological characteristics, we analyzed the human gastric cancer spatial transcriptomics cohort GSE251950. We enlisted a specialized pathologist to annotate the Lauren pathological classification for a total of 9 primary GC spatial transcriptome sections, categorizing them as diffuse type (GC2, GC6, GC9), intestinal type (GC1, GC3, GC5, GC8), or mixed type (GC4, GC7). Upon scoring the danger zone signature genes across these nine spatial transcriptome datasets, we observed that patients with diffuse or mixed subtypes exhibited higher danger zone scores compared to those with the intestinal subtype (Fig. 2d and e). At the spatial level, diffuse type patients, such as GC2, GC6 and GC9, exhibited clearly defined areas of high danger zone scores (Fig. 2f, g and h). However, patients with intestinal type did not show distinct high-scoring regions for the danger zone (Fig. 2i and j, Fig. S1b). Taken together, we validated the clinical relevance of the mouse spatial key region through integrated clinical pathology and human spatial transcriptomics. Notably, the spatial danger zone was most prominent in diffuse-type GC.

Considering the significant expression of immune and stromal marker genes in the danger zone, we next investigated whether the danger zone had an impact on TME of GC. Firstly, ESTIMATE algorithm revealed that danger zone score had the highest correlation with stromal score, immune score, as well as estimate score compared with other spatial clusters using ssGSEA score in ACRG cohort (Fig. 2k). In addition, the MCP-counter immune cell deconvolution algorithm demonstrated that danger zone score had the highest correlation with fibroblasts, endothelial cells and various immune cells (Fig. 2l). Therefore, we hypothesized that there might be intricate interactions between immune and stromal components within the spatial danger zone. To validate this hypothesis, we applied and annotated the GSE167297 gastric cancer single-cell RNA sequencing dataset and employed RCTD to map different cell types onto the spatial transcriptomics data of human gastric cancer. Subsequently, we calculated the proportion of immune cells as the sum of B cells, $CD8^+$ T cells, macrophages, mast cells, monocytes, plasma cells, $CD4^+$ T cells, and Tregs. The proportion of stromal cells was the sum of fibroblasts and endothelial cells, and the remaining proportion was considered epithelial cells (Fig. S2a). By conducting neighborhood network analysis, we established an interaction network between stromal and immune cells. Notably, in the spatial danger zone of GC6, a pronounced interaction network between stromal and immune cells was observed, while such interactions were significantly diminished in GC3 (Fig. 2m and n). Repeated analyses on other diffuse-type or intestinal-type samples yielded similar results (Fig. S2b, S2c).

Previous studies have led us to believe that the detrimental effects of TME components on immune cells often result in the ineffectiveness of ICI therapy [50, 51]. Therefore, our findings also encouraged us to investigate the impacts of danger zone on the ICI therapy of GC. First, clinical phenotype analysis from the ACRG indicated that patients with microsatellite stable (MSS) status exhibited higher danger zone scores (Fig. 2o), with MSS identified as one of the key factors associated with the ineffectiveness of ICIs in gastric cancer. Using the TIDE algorithm, we discovered that patients who did not respond to ICIs had a higher danger zone score (Fig. 2p). Moreover, the danger zone score exhibited a robust positive correlation with the Cancer-Associated Fibroblast (CAF) score, as well as the Dysfunction score derived from the TIDE algorithm (Fig. 2q). We then applied IMvigor210CoreBiologies, a cohort receiving PD-L1 blockage therapy with follow-up information, to validate the effect of the danger zone on ICI therapy. It was discovered that patients with higher danger zone score had worse overall survival (Fig. S2d). Additionally, patients with SD or PD as treatment outcomes also exhibited higher danger zone scores (Fig. S2e). Moreover, it was observed that danger zone score was negatively associated with neoantigens and FMOne mutation burden in IMvigor210 cohort (Fig. S2f). Collectively, the spatial danger zone exerted a substantial influence on the immune microenvironment of GC, potentially exacerbating immune dysfunction and leading to diminished efficacy of ICI therapy.

GC subtyping based on danger zone and a machine learning–based subtyping prediction

Considering the possible heterogeneity of danger zone among GC patients, we subsequently applied the danger zone marker genes to stratify patients in the ACRG cohort. Two distinct danger zone subtypes were clearly identified using NMF, with high silhouette scores (Fig. 3a). In addition, a total of 140 genes were filtered using the NMF algorithm, which were regarded as key differential markers between the two subtypes. Survival analysis revealed that patients in Subtype 2 had a worse prognosis, potentially attributable to their higher danger zone scores (Fig. 3b and c). Moreover, the stromal score and immune score in Subtype 2 were both higher than Subtype 1 (Fig. S3a). We also leveraged the CIBERSORT algorithm to reveal that the immune landscapes of Subtype 1 and Subtype 2 were distinct (Fig. S3b). Subtype 2 tended to have more M2 macrophage infiltration and lower proportions of activated dendritic cells, follicular helper T cells and activated memory $CD4^+$ T cells, suggesting a deficiency in antigen

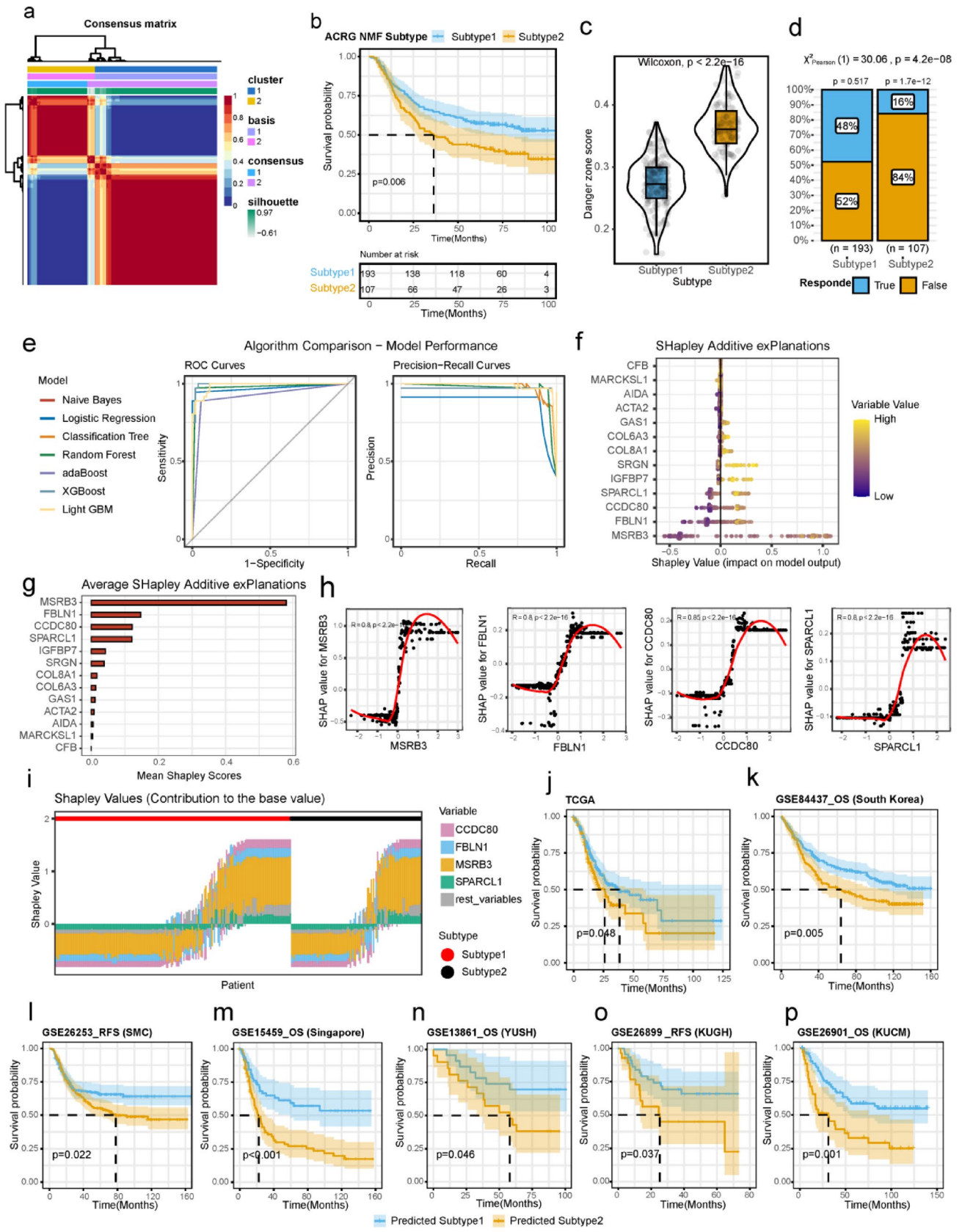
a
Consensus matrix
cluster
basis
consensus
silhouette
b
ACRG NMF Subtype
Subtype1
Subtype2
Survival probability
p=0.006
Time(Months)
Number at risk
Subtype1 193 138 118 60 4
Subtype2 107 66 47 26 3
c
Wilcoxon, p < 2.2e−16
Danger zone score
Subtype1
Subtype2
Subtype
d
X²Pearson (1) = 30.06 , p = 4.2e−08
p = 0.517
p = 1.7e−12
48%
52%
16%
84%
(n = 193)
(n = 107)
Subtype1
Subtype2
Responde
True
False
e
Algorithm Comparison − Model Performance
ROC Curves
Precision−Recall Curves
Model
Naive Bayes
Logistic Regression
Classification Tree
Random Forest
adaBoost
XGBoost
Light GBM
Sensitivity
1−Specificity
Precision
Recall
f
SHapley Additive exPlanations
CFB
MARCKSL1
AIDA
ACTA2
GAS1
COL6A3
COL8A1
SRGN
IGFBP7
SPARCL1
CCDC80
FBLN1
MSRB3
Variable Value
High
Low
Shapley Value (impact on model output)
g
Average SHapley Additive exPlanations
Mean Shapley Scores
h
SHAP value for MSRB3
SHAP value for FBLN1
SHAP value for CCDC80
SHAP value for SPARCL1
i
Shapley Values (Contribution to the base value)
Shapley Value
Patient
Variable
CCDC80
FBLN1
MSRB3
SPARCL1
rest_variables
Subtype
Subtype1
Subtype2
j
TCGA
p=0.048
k
GSE84437_OS (South Korea)
p=0.005
l
GSE26253_RFS (SMC)
p=0.022
m
GSE15459_OS (Singapore)
p<0.001
n
GSE13861_OS (YUSH)
p=0.046
o
GSE26899 _RFS (KUGH)
p=0.037
p
GSE26901_OS (KUCM)
p=0.001
Survival probability
Time(Months)
Predicted Subtype1
Predicted Subtype2

Fig. 3 Machine learning-based danger zone subtyping predicts prognosis and therapy response.**a** NMF-based identification of danger zone subtypes in the ACRG cohort. **b** Overall survival analysis comparing Subtype 1 and Subtype 2. **c** Quantification of danger zone scores between subtypes. **d** Predicted response to immune checkpoint inhibitors across subtypes. **e** ROC and PR curves of seven machine learning classifiers. **f** SHAP summary plot ranking the feature importance of 13 classifier genes. **g** Average SHAP value of 13 classifier genes. **h** Correlation between gene expression and SHAP values for top-ranked genes. **i** Patient-specific heterogeneity in SHAP contributions across genes. **j**,**k**,**m**, **n**,**p** Overall survival validation in independent cohorts: **j** TCGA, **k** GSE84437, **m** GSE15459, **n** GSE13861, and **p** GSE26901. **l**,**o** Recurrence-free survival (RFS) validation in **l** GSE26253 and **o** GSE26899

presentation and a prominent immunosuppressive microenvironment in Subtype 2. Regarding ICI therapy, patients in Subtype 2 had a poorer response rate compared with those in Subtype 1 (Fig. 3d). Furthermore, predicted chemotherapy drug sensitivities indicated that Subtype 2 patients exhibited markedly reduced responsiveness to agents such as methotrexate and paclitaxel (Fig. S3c). Taken together, Subtype 2, distinguished by high danger zone scores, had a poorer survival prognosis and a more pronounced immunosuppressive microenvironment.

To enable clinical application of danger zone subtyping, we aimed to construct a subtype classifier through machine learning. First, Boruta random forest was used to shrink the 140 NMF filtered genes to 34. Subsequently, 10-fold cross validation LASSO regression further reduced the genes to 13, including MARCKSL1, CFB, AIDA, SRGN, IGFBP7, ACTA2, SPARCL1, COL8A1, CCDC80, GAS1, MSRB3, COL6A3 and FBLN1. The chromosomal positions of the 13 genes, along with their distinctive patterns of copy number variation in gastric cancer, were also elucidated (Fig. S3d ,S3e). We then implemented an ensemble machine learning pipeline comprising seven methods: Naïve Bayes, Logistic Regression, Classification Tree, Random Forest, AdaBoost, XGBoost, and LightGBM. In the ACRG cohort, all of the 7 machine learning methods exhibited good predictive performance (Fig. 3e, Table S3). Among them, XGBoost achieved the best diagnostic performance (ROC-AUC = 0.9949, PR-AUC = 0.9915). Next, we used SHAP to explain the contribution of each gene for predicting danger zone subtypes in each sample. MSRB3, FBLN1, CCDC80 and SPARCL1 were the top four genes with the largest SHAP values (Fig. 3f and g). The expression levels of all four genes were positively correlated with Subtype 2 (danger zone high subtype). The SHAP values of these genes were also positively correlated with their expression levels (Fig. 3h). Moreover, SHAP analysis revealed inter-patient heterogeneity in the contribution of each gene's SHAP value (Fig. 3i). Furthermore, we substantiated the outstanding classification efficacy of the XGBoost model through validation in several independent cohorts. The overall survival rates across TCGA (Fig. 3j), GSE84437 (Fig. 3k), GSE15459 (Fig. 3m), GSE13861 (Fig. 3n), and GSE26901 (Fig. 3p) revealed significant disparities between the predicted subtypes. Remarkably, the follow-up mortality rate for Subtype 1 in several cohorts remained below 50%. Furthermore, distinct differences in disease-free survival rates were observed in GSE26253 (Fig. 3l), GSE26899 (Fig. 3o), and GSE26901 (Fig. S3h), corresponding to the predicted subtypes. For RFS in GSE13861 (Fig. S3f) and OS in GSE26899 (Fig. S3g), the XGBoost-based classification still showed a trend toward survival differences. These findings highlight the ability of the danger zone XGBoost classifier to distinguish patients with a higher risk of poor prognosis and recurrence.

Previous findings suggest that the danger zone is associated with lower tumor mutational burden (TMB) and reduced neoantigen load in GC. Given that the TCGA database encompasses simple nucleotide variation data and that the two subtypes of TCGA have been predicted, we utilized the Masked Somatic Mutation data from TCGA for validation. The waterfall plot and lollipop plot in the maftools package illustrated distinct mutation spectra for the two subtypes (Fig. S4a), highlighting differing mutation patterns and loci for key genes such as TP53 (Fig. S4b). Subtype 2 exhibited a significantly lower TMB and was more likely to be microsatellite stable (MSS) (Fig. S4c, S4d). COSMIC signature analysis revealed that, in addition to DNA mismatch repair deficiency, the mutational patterns in Subtype 2 were also associated with the spontaneous deamination of 5-methylcytosine (Fig. S4e).

CCDC80 in fibroblasts served as a key regulatory molecule in the danger zone

To further elucidate the cellular mechanisms underlying poor prognosis and immune suppression in the danger zone, we conducted an in-depth single-cell analysis of 13 classifier genes in GC. In the GSE167297 dataset, gene set scoring of the 13 classifier genes revealed that stromal cells, particularly fibroblasts, exhibited the highest scores (Fig. 4a). Upon further investigation of the cellular localization of the 13 genes, we observed that the majority were highly expressed in fibroblasts (Fig. 4b and c). To further explore the correlation between the danger zone and GC metastasis, we utilized dataset GSE163558, which includes samples from adjacent non-tumoral tissues (NT), primary tumor (PT), lymph node metastasis (LN), peritoneal metastasis (P), ovarian metastasis (O), and liver metastasis (Li) (Fig. S5a, S5b). Gene set scoring revealed that fibroblasts consistently exhibited the highest 13-gene score (Fig. 4d). Moreover, the fibroblast score was significantly elevated in tumor tissue compared to adjacent non-tumoral tissue (Fig. S5c). Among metastatic sites, fibroblasts in lymph

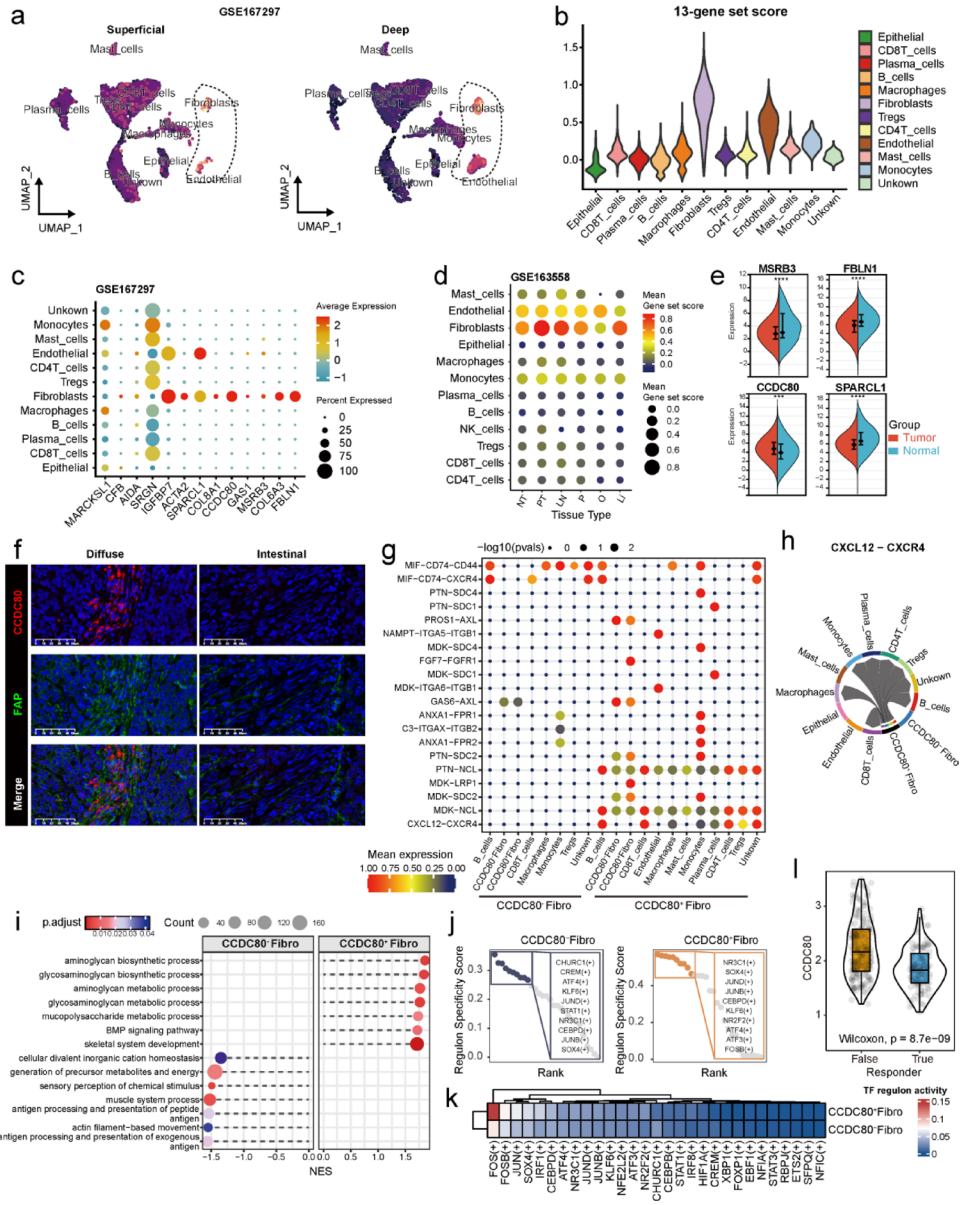

Fig. 4 CCDC80^{+} fibroblasts drive immune suppression and metastasis in the danger zone. (a) Expression profiling of 13 classifier genes across single-cell populations. **b-c** UMAP **b** and Dot plot **c** confirming fibroblast-specific enrichment of classifier genes. **d** Quantification of fibroblast gene signature scores in metastatic versus primary tumor sites. (**e** Differential expression analysis of key classifier genes in GC tumors versus normal tissues in TCGA-STAD, highlighting CCDC80. **f** Immunofluorescence co-localization of CCDC80 and fibroblasts (FAP^{+}) in diffuse-type and intestinal-type GC. **g** CellChat analysis of CCDC80^{+} fibroblasts and CCDC80^{-} fibroblasts with other cell types. **h** Key ligand-receptor pathways CXCL12-CXCR4. **i** GSEA of CCDC80^{+} and CCDC80^{-} fibroblasts. **j** RSS rank analysis of fibroblast-specific transcription factors in CCDC80^{-} and CCDC80^{+} fibroblasts by pySCENIC. **k** Transcription factor activity in CCDC80^{-} and CCDC80^{+} fibroblasts by pySCENIC. **l** Comparison of CCDC80 expression in predicted ICI responders and non-responders based on TIDE algorithm

node and liver metastases demonstrated the highest score (Fig. 4d, Fig. S5d, S5e). These findings suggest that danger zone–mediated mechanisms may contribute to tumor progression across diverse metastatic sites in GC. To identify the most critical genes among the 13, we examined the differential expression of the top four SHAP-ranked genes—MSRB3, FBLN1, CCDC80, and SPARCL1—in bulk transcriptomic data from TCGA-STAD and adjacent non-tumoral tissues. Notably, only CCDC80 showed elevated expression in tumor tissues, suggesting it may be the most robust and functionally relevant among the classifier genes (Fig. 4e). Furthermore, we conducted immunofluorescence on samples from GC patients and observed significant co-localization of fibroblasts (marked by FAP) and CCDC80 in diffuse-type GC, with a co-localization index of 0.75 (Fig. 4f, Fig. S5f). In contrast, such co-localization was less prevalent in intestinal-type patients. This further validated the significant presence of the danger zone in diffuse-type gastric cancer.

Subsequently, we categorized fibroblasts into two groups: those with CCDC80 expression (CCDC80^{+} fibroblasts) and those with no expression (CCDC80^{-} fibroblasts). The CellChat package was employed to examine the differences in cell-cell communication between CCDC80^{+} fibroblasts and CCDC80^{-} fibroblasts. We found that CCDC80^{+} fibroblasts engaged in more ligand-receptor signaling with CD8^{+} T cells, B cells, and other immune cells, particularly through pathways such as CXCL12-CXCR4, MDK-NCL, and PTN-NCL (Fig. 4g and h, Fig. S5g). Additionally, by extracting the differentially expressed genes between CCDC80^{+}

fibroblasts and CCDC80$^-$ fibroblasts and performing GSEA, we found that CCDC80$^+$ fibroblasts were primarily enriched in pathways such as the aminoglycan biosynthetic process and glycosaminoglycan biosynthetic process, but showed a loss of antigen presentation-related pathways (Fig. 4i). Moreover, pySCENIC transcription factor analysis revealed distinct specific transcription factors between CCDC80$^-$ and CCDC80$^+$ subsets (Fig. 4j). Transcription factor activity further indicated that CCDC80$^+$ fibroblasts exhibit higher average activity of FOS and FOSB (Fig. 4k), which were also identified as a highly specific transcription factor of CCDC80$^+$ fibroblasts (Fig. 4j). From the bulk cohort perspective, it was notable that CCDC80 expression was elevated in patients predicted by TIDE to be non-responders to ICIs (Fig. 4l). Moreover, CCDC80 consistently demonstrated a strong association with poor prognosis across multiple cohorts (Fig. S6a). The proportion of CCDC80$^+$ to CCDC80$^-$ fibroblasts was positively correlated with TIDE scores (Fig. S6b), suggesting that CCDC80$^+$ fibroblasts may contribute to immune checkpoint inhibitor resistance in GC. As spatial danger zones were initially identified using KRAS-mutant murine gastric tumors, we subsequently evaluated the correlation between Ras signaling pathway activity and CCDC80 expression in the ACRG and TCGA cohorts. A clear positive association was observed, suggesting a potential link to sustained Ras signaling activation driven by KRAS mutations (Fig. S6c).

To assess whether the spatial danger zone observed in gastric cancer might also emerge in related tumor types, we applied the danger-zone scoring framework to spatial transcriptomic datasets from colorectal cancer. In poorly differentiated samples, the danger zone prominently encircled the tumor nests (Fig. S6d, left), a pattern distinct from the intertumoral distribution seen in gastric cancer. In well-differentiated samples, however, danger-zone signals were minimal (Fig. S6d, right, Fig. S6e). In small bowel adenocarcinoma—a rare malignancy within the digestive system—the danger zone was likewise elevated in tumor regions (Fig. S6f) and showed strong positive correlations with both CCDC80$^+$ fibroblast infiltration and CCDC80 expression (Fig. S6g). These findings suggest that the danger zone is not unique to gastric cancer and may be driven by a conserved mechanism centered on CCDC80$^+$ fibroblasts, although its spatial configuration varies across tumor types.

CCDC80$^+$ fibroblasts exert a more pronounced effect on CD8$^+$ T cells in spatial level

To further investigate the roles of CCDC80$^+$ fibroblasts compared to CCDC80$^-$ fibroblasts within the immune microenvironment in spatial level, we employed RCTD deconvolution to calculate the proportions of CCDC80$^+$ fibroblasts, CCDC80$^-$ fibroblasts, and other cell types in spatial transcriptomics data from diffuse-type (GC6) and intestinal-type (GC3) human GC samples. Using the SPOTlight package to calculate spatial correlations between various cell types, we found that CCDC80$^+$ fibroblasts exhibited stronger spatial correlations with immune cells, including B cells and CD8$^+$ T cells, compared to CCDC80$^-$ fibroblasts (Fig. 5a and b). This effect was particularly pronounced in diffuse-type gastric cancer, aligning with the earlier findings from single-cell communication analysis. MistyR spatial colocalization analysis revealed that in diffuse-type gastric cancer, CCDC80$^+$ fibroblasts exhibited stronger colocalization with CD8$^+$ T cells at both intra- and juxta-cellular distances, while differences with other immune cells were less pronounced (Fig. 5c and d). Interestingly, in the intestinal-type spatial transcriptomics, CCDC80$^+$ fibroblasts did not show enhanced colocalization with CD8$^+$ T cells (Fig. 5e and f, Fig. S7a-S7d). SpatialFeaturePlot also confirmed the colocalized expression of CCDC80$^+$ fibroblasts and CD8$^+$ T cells in danger zone in GC6 (Fig. 5g and h). Focusing on CD8$^+$ T cells, we further employed neighborhood cell network analysis and discovered that CCDC80$^+$ fibroblasts tended to form an encapsulating structure around CD8+T cells within the danger zone, a pattern that was clearly observed in diffuse-type gastric cancer but not as evident in the intestinal-type (Fig. 5i and j). Repeated analyses on additional intestinal-type and diffuse-type samples (GC2, GC8) consistently revealed a stronger correlation between CCDC80$^+$ fibroblasts and CD8$^+$ T cells in the diffuse type, along with more pronounced interaction patterns within the danger zone (Fig. S7e-S7h). Moreover, using the COMMOT spatial signaling flow analysis, we identified a significant CXCL12-CXCR4 ligand-receptor signaling axis within the danger zone (Fig. 5k, Fig. S7i). This signaling may underlie the mechanism by which CCDC80$^+$ fibroblasts recruit and encapsulate CD8$^+$ T cells. In intestinal-type patients, the spatial signaling flux between CXCL12 and CXCR4 was relatively weak (Fig. S7j, S7k). However, the MDK-NCL signaling pathway did not exhibit the characteristic pattern of the danger zone (Fig. S7l, S7m). Immunofluorescence further indicated that fibroblasts expressing CCDC80 also displayed substantial levels of CXCL12 (Fig. 5l). In summary, spatial transcriptomic analysis suggested that CCDC80$^+$ fibroblasts recruit CD8$^+$ T cells via the CXCL12–CXCR4 signaling axis, thereby contributing to their functional impairment.

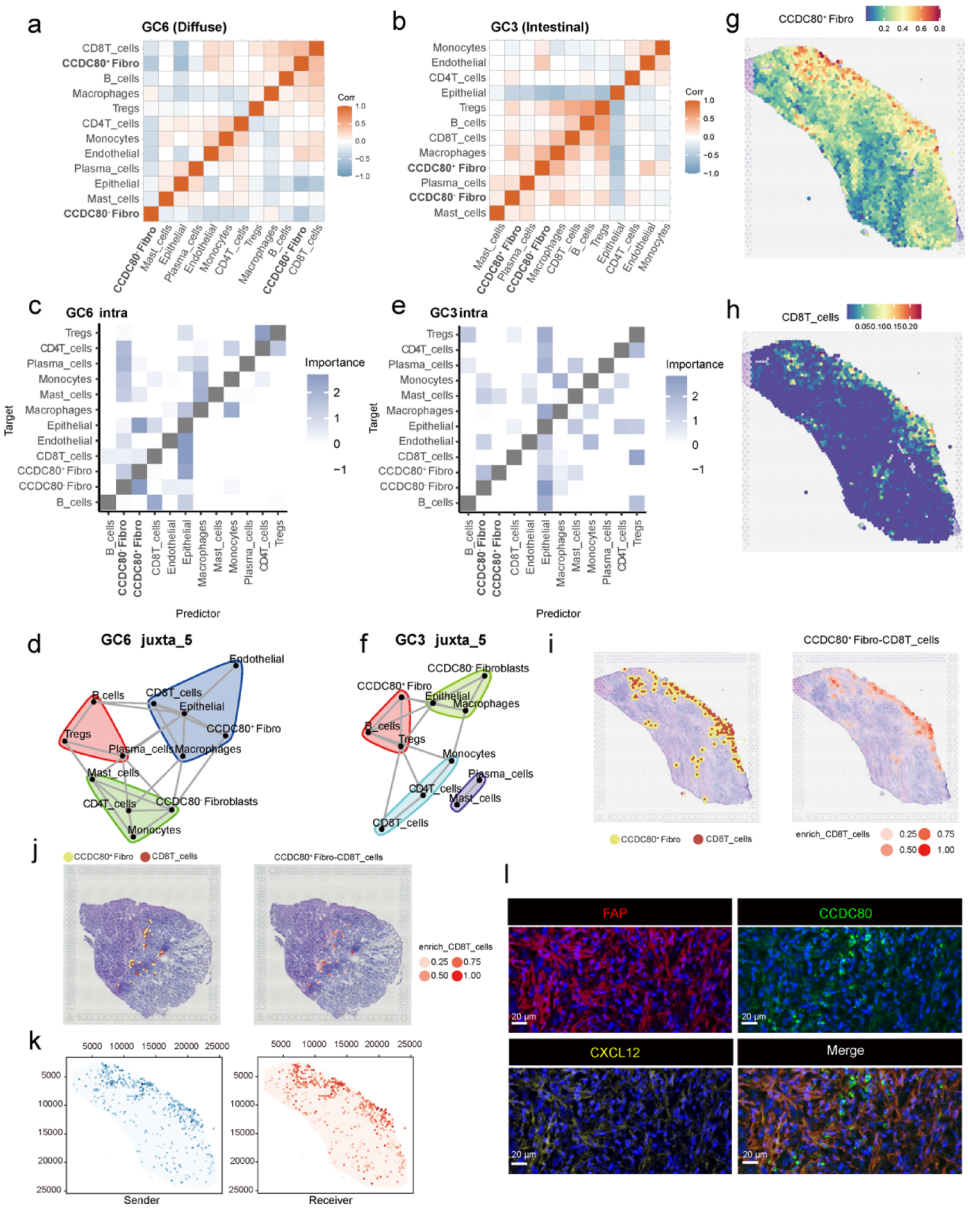

Fig. 5 Spatial encapsulation of CD8$^+$ T cells by CCDC80$^+$ fibroblasts via CXCL12-CXCR4 signaling. **a-b** Spatial correlation analysis using SPOTlight for CCDC80$^+$ fibroblasts and immune cell subsets in **a** diffuse-type (GC6) and **b** intestinal-type (GC3). **c-d** MistyR colocalization analysis of **c** intra and **d** juxta-cellular proximity of CCDC80$^+$ fibroblasts to CD8$^+$ T cells in diffuse-type GC (GC6). **e-f** MistyR colocalization analysis of **e** intra and **f** juxta-cellular proximity of CCDC80$^+$ fibroblasts to CD8$^+$ T cells in intestinal-type GC (GC3). **g-h** SpatialFeaturePlot of **g** CCDC80$^+$ fibroblasts and **h** CD8$^+$ T cells in diffuse-type GC (GC6). **i-j** Neighborhood network analysis of CCDC80$^+$ fibroblasts and CD8$^+$ T cells in **i** diffuse-type and **j** intestinal-type GC. **k** COMMOT-based signaling flux analysis of CXCL12–CXCR4 ligand–receptor axis. **l** Immunofluorescence detection of CXCL12 expression in CCDC80$^+$ fibroblasts

Recruitment of effector CD8$^+$ T cells to the danger zone followed by exhausted release into the tumor area

To further clarify the specific forms of CD8$^+$ T cells recruited and released in the danger zone, we first classified CD8$^+$ T cells at the single-cell level into effector CD8$^+$ T cells (CD8_eff) and exhausted CD8$^+$ T cells (CD8_exhau), and then deconvoluted these subtypes into the spatial transcriptomic data (Fig. S8a, S8b). We observed that the T cell population within the danger zone was predominantly composed of CD8_eff, whereas CD8_exhau were diffusely distributed at the periphery of the danger zone and within the tumor region (Fig. 6a). This suggested that the danger zone predominantly captured CD8_eff. Subsequently, we ranked the top 10% of spots based on the proportions of CD8_eff and CD8_exhau in the spatial transcriptomics data, designating them as CD8_eff and CD8_exhau, respectively. We then performed spatial CellChat analysis to explore cell-cell communication. We found that, within the CXCL signaling pathway, CCDC80$^+$ fibroblasts exhibited stronger communication with CD8_eff cells than with CD8_exhau cells, and also stronger than the communication between CCDC80$^-$ fibroblasts and CD8$^+$ T cells (Fig. 6b and c). This further validated that CD8_eff were the predominant cells entering the danger zone. Interestingly, we found that the CXCL12–CXCR4 signaling pathway was exclusively active in CCDC80$^+$ fibroblasts and interacted with both CD8_eff and CD8_exhau cells, suggesting that CXCL12 may not only promote the recruitment and retention of CD8$^+$ T cells but

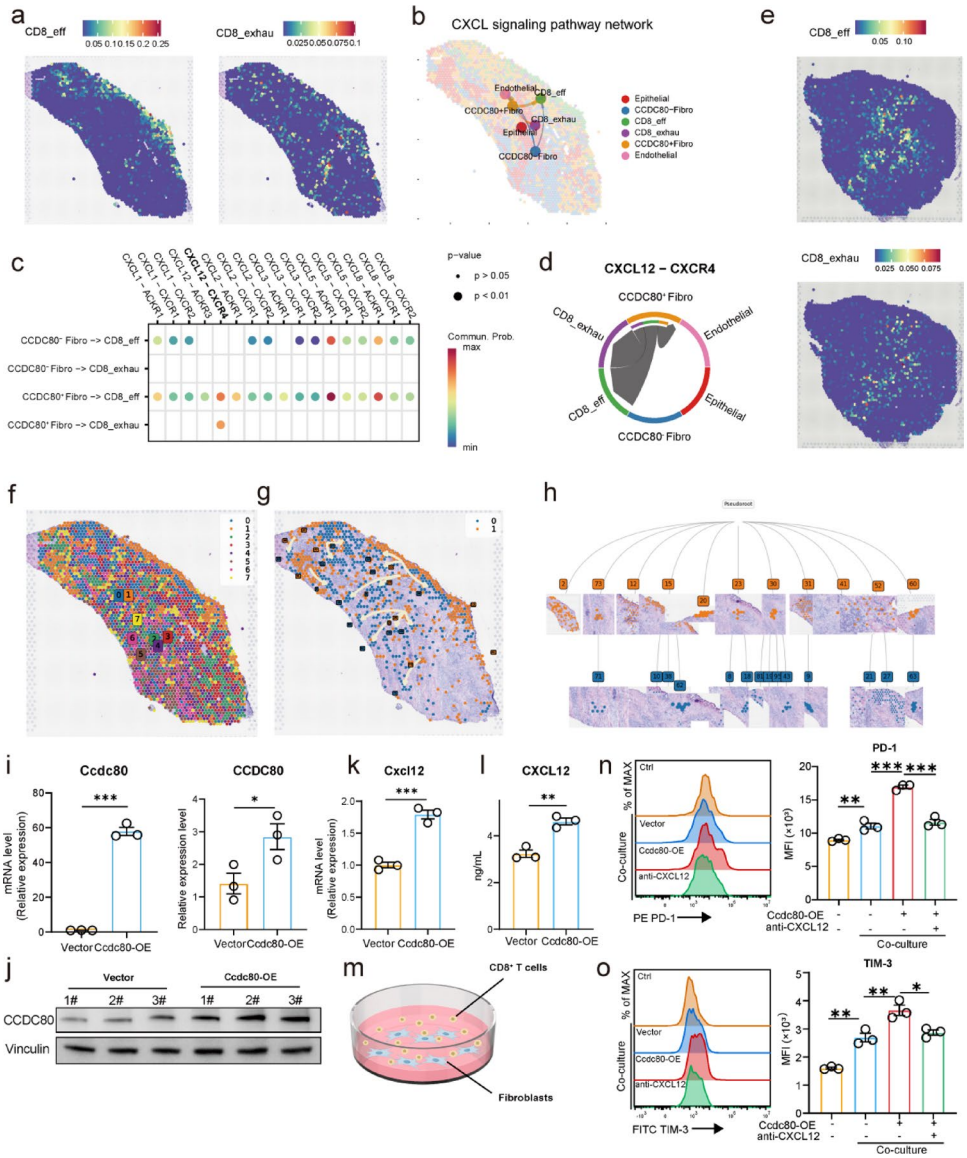

Fig. 6 CCDC80$^+$ fibroblasts recruit effector CD8$^+$ T cells into the danger zone and drive their exhaustion via CXCL12. **a** Spatial deconvolution of effector CD8$^+$ T cells (CD8_eff) and exhausted CD8$^+$ T cells (CD8_exhau). **b** Spatial CellChat analysis of CXCL signaling between CD8$^+$ T cell subsets and CCDC80$^+$ or CCDC80$^-$ fibroblasts. **c** Bubble plot of ligand-receptor pairs between CD8$^+$ T cell subsets and CCDC80$^+$ or CCDC80$^-$ fibroblasts. **d** Ligand–receptor interaction analysis showing exclusive engagement of CCDC80$^+$ fibroblasts in CXCL12–CXCR4 signaling with both CD8_eff and CD8_exhau cells. **e** Quantification of CD8_eff and CD8_exhau recruitment in intestinal-type GC (GC3). **f** Spatial clustering of GC6 sample. **g** Pseudotime trajectory from cluster 1 to cluster 0. **h** Representative trajectory (15 − 10/38/62) demonstrating spatial progression to exhaustion. **i** qRT-PCR for CCDC80 mRNA expression in NIH-3T3 fibroblasts. **j** Immunoblot for CCDC80 protein expression. **k** qRT-PCR for CXCL12 mRNA in CCDC80-overexpressing fibroblasts. **l** ELISA for quantification of CXCL12 secretion. **m** Schematic of fibroblast-CD8$^+$ T cell co-culture experiment. **n** Flow cytometry for PD-1 expression on CD8$^+$ T cells with or without CXCL12 blockade. **o** Flow cytometry for TIM-3 expression on CD8$^+$ T cells with or without CXCL12 blockade

also contribute to their functional exhaustion (Fig. 6d). In intestinal-type patients, CD8_eff cells were also enriched within the danger zone, although their overall infiltrative density was relatively low. Furthermore, exhausted CD8$^+$ T cells tended to avoid entering the tumor area (Fig. 6e). This suggested that the T cell recruitment and exhaustion effects in the danger zone of intestinal-type patients were relatively weaker. To further confirm whether CD8_exhau were developed from the CD8_eff, we performed stlearn developmental trajectory analysis. Compared to Fig. 6a, we found that the purple CD8_exhau cells tended to be distributed at the outer side of the danger zone, specifically in cluster 0, while the danger zone was represented by cluster 1 (Fig. 6f). The developmental trajectory analysis indicated a developmental progression from cluster 1 to cluster 0, suggesting that the exhausted CD8$^+$ T cells infiltrating the tumor might indeed originate from the danger zone (Fig. 6g). For example, the developmental trajectory 15 − 10/38/62 represented a typical spatial developmental trajectory from the danger zone to the outer side (Fig. 6h).

To investigate whether CCDC80 induces exhaustion of activated CD8$^+$ T cells by upregulating CXCL12 expression, we overexpressed the Ccdc80 gene in the murine fibroblast cell line NIH-3T3. Successful overexpression was confirmed at both the mRNA and protein levels (Fig. 6i and j), as well as immunofluorescence (Fig. S8c). Subsequent qRT-PCR and ELISA analyses demonstrated that CCDC80 overexpression significantly increased CXCL12 expression in these fibroblasts (Fig. 6k and l). Next, CD8$^+$ T cells were isolated from the spleens of C57BL/6 mice and activated using anti-CD3/CD28 antibodies. The activated T cells were then co-cultured for 24 h with either CCDC80-overexpressing fibroblasts or control fibroblasts (Fig. 6m). The results showed that overexpression of Ccdc80 in fibroblasts

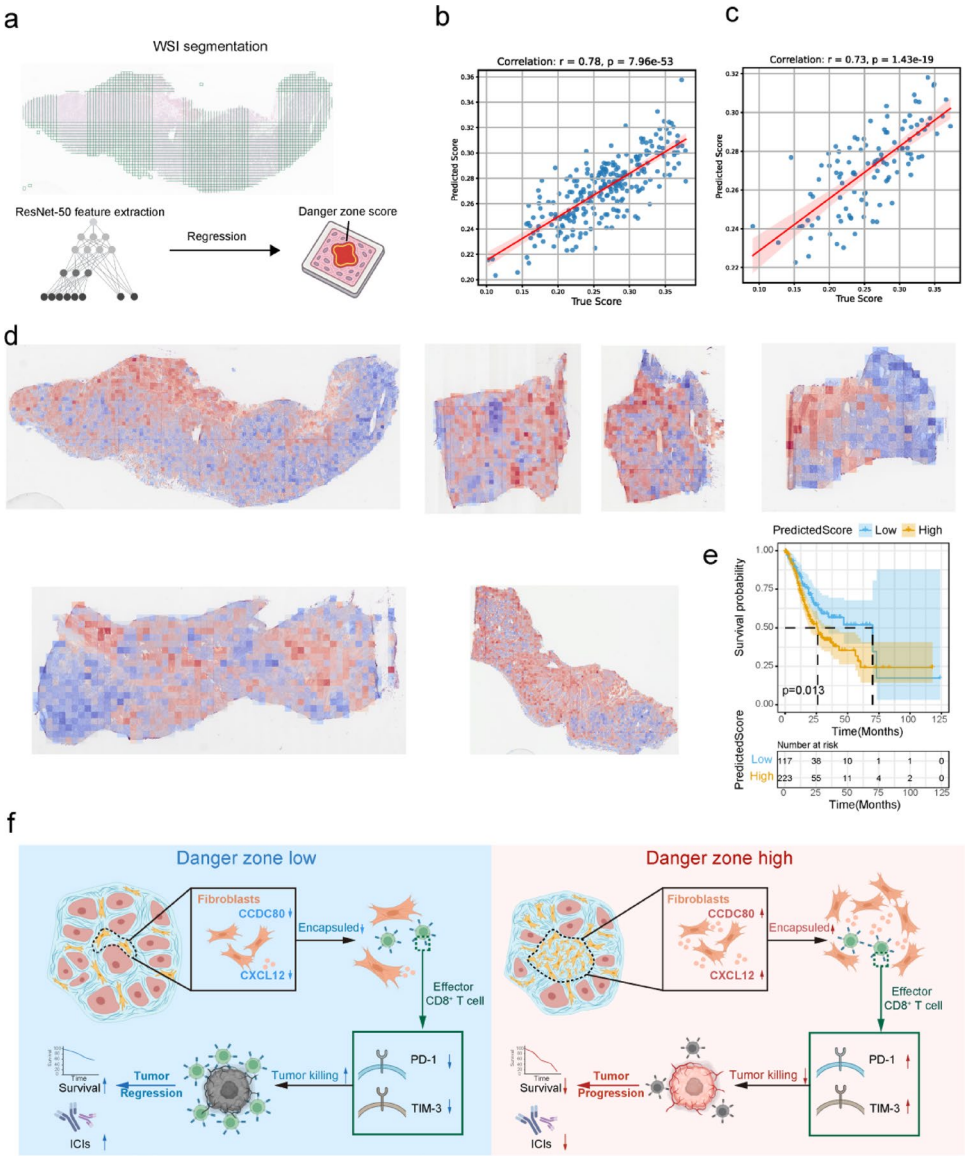

Fig. 7 H&E-based prediction of danger zone scores. **a** Workflow for the WSI tiling, feature extraction, and model construction. **b** Correlation analysis of predicted versus true danger zone scores in training set ($n=254$). **c** Correlation analysis of predicted versus true danger zone scores in testing set ($n=110$). **d** Visualization of patch-wise predicted risk scores projected onto whole slide images. **e** Survival analysis showing association between predicted danger zone scores and overall survival in the TCGA-STAD cohort ($n=340$). **f** Proposed mechanistic model of this study

markedly upregulated exhaustion markers, including PD-1 and TIM-3, on $CD8^+$ T cells (Fig. 6n and o). Notably, the addition of a CXCL12-neutralizing antibody reversed this exhaustion phenotype, indicating that the effect was mediated through CXCL12 (Fig. 6n and o). These findings collectively demonstrate that fibroblast-derived CCDC80 can promote exhaustion of activated $CD8^+$ T cells via upregulation of CXCL12.

Prediction of danger zone scores using H&E-stained pathology slides

To provide a more convenient method for assessing patient danger zone scores, we obtained Whole Slide Images (WSIs) for patients in the TCGA-STAD cohort. Using Histolab, we performed grid-based tiling of the WSIs and extracted 2048-dimensional deep learning features from each image patch using ResNet-50 (Fig. 7a). In total, we collected 378,513 pathology image patches from 364 patients. The dataset was divided into a training set of 254 patients and a validation set of 110 patients. We constructed a regression model using LightGBM regressor based on pathological features and outcome-derived danger zone scores. In the training set, the predicted scores showed strong correlations with the true scores, with a Pearson correlation coefficient of 0.7781 (Fig. 7b), a Spearman correlation coefficient of 0.7617, an RMSE of 0.0419, and an R^2 of 0.4732. In the testing set, the Pearson and Spearman correlation coefficients were 0.7302 (Fig. 7c) and 0.7249, respectively, with an RMSE of 0.0463 and an R^2 of 0.3575, indicating acceptable model stability. To further interpret the model's predictions, we visualized the predicted scores for each image patch on the pathology slides. Interestingly, patches with

high predicted scores were predominantly located in stromal regions with high infiltration of fibroblast-like cells, whereas regions with high tumor purity tended to have lower predicted scores (Fig. 7d). This pattern was consistently observed across different samples. Importantly, among the 340 patients with available prognostic information, the predicted danger zone score was a significant adverse prognostic factor (Fig. 7e), suggesting that this pathology-based score prediction model may serve as a promising prognostic indicator in clinical practice. In summary, the principal findings of this study are illustrated in the mechanistic diagram (Fig. 7f): in gastric cancer patients with a high spatial distribution of the danger zone, elevated CCDC80 expression in fibroblasts within this zone drives CXCL12 overexpression, which can encapsulate and sequester $CD8^+$ T cells, leading to their exhaustion. This, in turn, promotes tumor progression and contributes to poor responses to immune checkpoint blockade. In contrast, the opposite pattern is observed in patients with a low distribution of the danger zone.

Discussion

Given that surgical resection remains the cornerstone of curative treatment for gastric cancer, understanding the spatial biology of postoperative tumor specimens is essential for improving patient stratification and therapeutic decision-making. Although the global incidence and mortality rates for gastric cancer have declined, it remains one of the most common types of cancer, with particularly high incidence in East Asian countries, accounting for over 70% of new diagnoses and deaths worldwide. Adenocarcinoma is the predominant type of gastric cancer, representing over 95% of cases [52]. Despite significant advances in diagnostic and therapeutic strategies in recent years, which have markedly improved patient survival rates, regional risk studies focusing on spatial transcriptomics in gastric cancer are still limited. Our research on spatial transcriptomic profiling of gastric adenocarcinoma revealed a distinct "danger zone" in gastric cancer, particularly in diffuse gastric cancer, where the aggregation of stromal and immune cells was significantly increased. Analysis of the crosstalk between stromal and immune cells in the danger zone demonstrated that $CCDC80^+$ fibroblasts induced the exhaustion of $CD8^+$ T cells, leading to localized tumor progression and resistance to immunotherapy. In summary, we explored potential factors contributing to tumor occurrence and progression in gastric cancer risk areas, aiming to provide new insights into the disease mechanisms and treatment approaches.

In our study, we observed that tumor cells in the spatial danger zone of gastric cancer exhibit significantly strengthened interactions with immune cells and stromal cells including fibroblasts and endothelial cells. Importantly, the area where the crosstalk between stromal and immune cells was most active spatially overlapped highly with the danger zone. This indicated a close relationship between tumor cells, stromal cells, and immune cells within the spatial danger zone. While research into immune cell-tumor cell interactions has deepened, the interactions between stromal cells and TME also merit further investigation. Previous studies have found that fibroblasts have a tumor-promoting role across various cancers. Research clustering tumor-associated fibroblasts into 23 clusters reveals that, although their distribution varies across cancers, six clusters show high similarity, suggesting shared signaling pathways that promote tumor progression [53]. Endothelial cells, crucial components of the tumor microenvironment, facilitate angiogenesis and cell movement in gastric cancer but hinder antigen presentation and immune defense pathways. Activated endothelial cells are linked to worsened survival rates in gastric cancer, making them potential targets to prevent metastasis [54]. Another study found that FAP^+ fibroblasts and $SPP1^+$ macrophages in colorectal cancer correlate strongly with patient survival, with their coexistence promoting fibrotic structures and resistance to PD-L1 blockade immunotherapy [55]. Additionally, recent research highlights interactions between stromal and immune cells in gastric cancer. A 2023 study showed fibroblasts and endothelial cells had negative correlations with $CD4^+$/$CD8^+$ T cells [56]. Overall, these studies indicate that extensive stromal remodeling significantly impacts gastric cancer progression and treatment. However, most previous research has focused on cellular interactions without addressing the spatial dimension of cell crosstalk and its impact on patient prognosis, which our study aims to address.

We ultimately focused on the gene CCDC80 (coiled-coil domain containing 80, also known as DRO1, SSG1, and URB) through diagnostic models, expression levels, and cell localization. The role of CCDC80 in tumors is still somewhat controversial. Earlier studies suggested that CCDC80 might act as a protective factor in tumorigenesis [57–59]. For example, in thyroid cancer research, CCDC80 expression was found to be significantly lower in almost all analyzed thyroid cancer samples compared to normal thyroid tissue, with the lowest expression in follicular variant papillary thyroid cancer. Restoration of CCDC80 expression in two human anaplastic thyroid cancer cell lines increased susceptibility to apoptosis and suppression of malignant phenotypes, indicating that CCDC80 could be a potential tumor suppressor gene in thyroid cancer [58]. However, recent studies report that in colorectal cancer, CCDC80 may increase tumor drug resistance and immune evasion [60]. Another study indicated that high CCDC80 expression in advanced CRC was associated with poorer prognosis, as

increased CCDC80 levels led to oxaliplatin chemoresistance and distant liver metastasis, while inhibition of CCDC80 significantly enhanced CRC cell sensitivity to OXA-based chemotherapy [61]. Our study found that CCDC80$^+$ fibroblasts recruited and retained CD8$^+$ T cells in the danger zone via the CXCL12-CXCR4 pathway and induced their exhaustion, leading to tumor progression and immunotherapy resistance within the danger zone. CXCL12, also known as stromal cell-derived factor-1, is a small secreted chemokine belonging to the C-X-C subfamily, with a molecular weight of approximately 8 kDa and containing two conserved cysteine residues [62, 63]. Its primary receptor, CXCR4—formerly referred to as fusin or leukocyte-derived seven-transmembrane receptor—is a classic seven-transmembrane G protein-coupled receptor [64]. Upon binding of CXCL12 to the extracellular domain of CXCR4, the associated Gα subunit undergoes activation via GDP–GTP exchange, leading to the production of cyclic AMP [65]. This event triggers multiple downstream signaling pathways, including Akt, JNK, MEK, and ERK1/2, resulting in transcriptional changes that promote integrin clustering, actin cytoskeleton reorganization, pseudopodia formation, and intracellular calcium release—ultimately facilitating directional chemotaxis of lymphocytes [65]. Following ligand engagement, CXCR4 is commonly ubiquitinated and subsequently internalized for lysosomal degradation [66]. Under physiological conditions, the CXCL12–CXCR4 axis plays a vital role in directing hematopoietic progenitor cells and differentiated lymphocytes to their target locations. Additionally, CXCL12 binding enhances leukocyte adhesion to intercellular adhesion molecule-1 (ICAM-1) and vascular cell adhesion molecule-1 (VCAM-1) by stabilizing integrin interactions, enabling firm adhesion after the initial rolling phase within the vasculature [67]. Studies in gastric cancer have shown that CXCL12 secretion facilitates the migration of CAFs toward tumor regions. Compared to normal gastric fibroblasts, CAFs derived from gastric cancer tissues exhibit significantly higher levels of CXCL12 expression [68–71]. One study indicated that CD14$^+$ CD8$^+$ T cells are tissue-resident cells with high expression of CXCR3, CXCR4, CD49a, and CD49b [72], while another reported that CXCR4, rather than CXCR3, was crucial for the homing of all CD8$^+$ T cell subsets in mice [73]. These studies indirectly corroborate our findings, suggesting that CCDC80$^+$ fibroblasts recruit CD8$^+$ T cells to the stromal danger zone through the secretion of CXCL12, while CXCR4 expressed on the surface of CD8$^+$ T cells further mediates their retention within this stromal danger zone. Transcription factor analysis further suggests that FOSB may be a key regulator mediating CCDC80-induced upregulation of CXCL12. Previous studies have also reported an important link between FOS/FOSB and CXC chemokine regulation [74, 75].

In our study, we further revealed that aberrant CXCL12–CXCR4 interactions between CCDC80$^+$ fibroblasts and CD8$^+$ T cells led to the entrapment of CD8$^+$ T cells within the spatial danger zone, leading to their apoptosis. Supporting our findings, a recent study in bladder cancer reported that cancer-associated fibroblast-derived CXCL12 acted on tumor cells to upregulate the expression of the deubiquitinating enzyme CYLD. This, in turn, promoted p62 accumulation via deubiquitination and inhibited the autophagic degradation of PD-L1. The stabilized PD-L1 on the tumor cell surface then engaged PD-1 receptors on CD8$^+$ T cells, suppressing their cytotoxic function. In vivo experiments further confirmed that blockade of CXCL12 suppressed tumor growth, reduced PD-L1 expression in tumor tissues, and enhanced immune cell infiltration [76]. These findings are consistent with our observations, suggesting that fibroblast-derived CXCL12 plays a crucial role in suppressing CD8$^+$ T cell activity and mediating tumor immune evasion. Although our spatial transcriptomics analysis did not reveal a significant spatial association between the MDK pathway and the danger zone, single-cell analysis identified significant cell–cell communication between CCDC80$^+$ fibroblasts and CD8$^+$ T cells, suggesting that the MDK pathway may also play a role in regulating CD8$^+$ T cell function. A study showed that the MDK pathway played a significant role in tumor cells evading CD8$^+$ T cell immune surveillance, deceiving the host immune system, and increasing resistance to chemotherapy. This mechanism involved the MDK pathway regulating secreted proteins in melanoma to induce a macrophage phenotype that promotes CD8$^+$ T cell dysfunction and resistance to PD-1/PD-L1 therapy [77].

This study also has several limitations. At present, only the KRAS^{G12V}-expressing and p53-knockout gastric neoplasia mouse model was used. Future spatial transcriptomic profiling of additional highly invasive gastric cancer mouse models will strengthen the generalizability of our conclusions. Second, the functional role of CCDC80 was primarily inferred from transcriptomic data, without systematic validation of CCDC80 protein expression levels in large gastric cancer cohorts. Additionally, although the CCDC80–CXCL12 axis was preliminarily verified through in vitro co-culture experiments, its function within the in vivo tumor microenvironment still requires further confirmation using animal models.

Conclusion

In summary, our study identifies a spatially defined danger zone in gastric adenocarcinoma, characterized by the presence of CCDC80$^+$ fibroblasts that recruit and induce exhaustion of CD8$^+$ T cells through the CXCL12–CXCR4

axis. These findings not only highlight CCDC80^{+} fibroblasts as a potential therapeutic target to overcome immune evasion but also lay the foundation for developing spatial danger zone-based scoring systems to predict patient prognosis and the efficacy of ICI therapy in gastric cancer.

Supplementary Information The online version contains supplementary material available at https://doi.org/10.1007/s10495-026-02287-1.

Acknowledgements Not applicable.

Author contributions SM contributed to data analysis and study design. YW contributed to manuscript writing. RX contributed to experimental validation. LM contributed to literature review. MX was responsible for sample collection. LW supervised the study. WG provided methodological support and supervision.

Funding This work was supported by the National Natural Science Foundation of China (Grant No. 823B2082), the Japan Society for the Promotion of Science (JSPS) KAKENHI (Grant Nos. JP24K18786 and JP22K20814), and the Takeda Science Foundation (Grant No. 2024041296).

Data availability No datasets were generated or analysed during the current study.

Declarations

Ethics approval and consent to participate The animal experiments have received ethical approval (No.: IACUC-2025-NI-029), and the inclusion of human samples has obtained ethical approval (No.: 050432-4-2307E).

Consent for publication Not applicable.

Competing interests The authors declare no competing interests.

References

1. Joshi SS, Badgwell BD (2021) Current treatment and recent progress in gastric cancer. CA Cancer J Clin 71:264–279
2. Allen CJ, Blumenthaler AN, Smith GL et al (2021) Chemotherapy versus chemotherapy plus chemoradiation as preoperative therapy for resectable gastric adenocarcinoma: a propensity Score-Matched analysis of a Large, Single-Institution experience. Ann Surg Oncol 28:758–765
3. Marabelle A, Le DT, Ascierto PA et al (2020) Efficacy of pembrolizumab in patients with noncolorectal high microsatellite Instability/Mismatch Repair-Deficient cancer: results from the phase II KEYNOTE-158 study. J Clin Oncol 38:1–10
4. Lee J, Lim DH, Kim S et al (2012) Phase III trial comparing capecitabine plus cisplatin versus capecitabine plus cisplatin with concurrent capecitabine radiotherapy in completely resected gastric cancer with D2 lymph node dissection: the ARTIST trial. J Clin Oncol 30:268–273
5. van Hagen P, Hulshof MC, van Lanschot JJ et al (2012) Preoperative chemoradiotherapy for esophageal or junctional cancer. N Engl J Med 366:2074–2084
6. Bang YJ, Van Cutsem E, Feyereislova A et al (2010) Trastuzumab in combination with chemotherapy versus chemotherapy alone for treatment of HER2-positive advanced gastric or gastro-oesophageal junction cancer (ToGA): a phase 3, open-label, randomised controlled trial. Lancet 376:687–697
7. Gwee YX, Chia DKA, So J et al (2022) Integration of genomic biology into therapeutic strategies of gastric cancer peritoneal metastasis. J Clin Oncol 40:2830
8. Tang D, Liu S, Shen H, Deng G, Zeng S (2022) Extracellular vesicles promote the formation of Pre-Metastasis niche in gastric cancer. Front Immunol 13:813015
9. Derks S, de Klerk LK, Xu X et al (2020) Characterizing diversity in the tumor-immune microenvironment of distinct subclasses of gastroesophageal adenocarcinomas. Ann Oncol 31:1011–1020
10. Kumar V, Ramnarayanan K, Sundar R et al (2022) Single-Cell atlas of lineage States, tumor Microenvironment, and Subtype-Specific expression programs in gastric cancer. Cancer Discov 12:670–691
11. Wang R, Dang M, Harada K et al (2021) Single-cell dissection of intratumoral heterogeneity and lineage diversity in metastatic gastric adenocarcinoma. Nat Med 27:141–151
12. Jeong HY, Ham IH, Lee SH et al (2021) Spatially distinct reprogramming of the tumor microenvironment based on tumor invasion in Diffuse-Type gastric cancers. Clin Cancer Res 27:6529–6542
13. Wang J, Kunzke T, Prade VM et al (2022) Spatial metabolomics identifies distinct Tumor-Specific subtypes in gastric cancer patients. Clin Cancer Res 28:2865–2877
14. Koh V, Chakrabarti J, Torvund M et al (2021) Hedgehog transcriptional effector GLI mediates mTOR-Induced PD-L1 expression in gastric cancer organoids. Cancer Lett 518:59–71
15. Sun C, Wang A, Zhou Y et al (2023) Spatially resolved multi-omics highlights cell-specific metabolic remodeling and interactions in gastric cancer. Nat Commun 14:2692
16. Cui Zhou D, Jayasinghe RG, Chen S et al (2022) Spatially restricted drivers and transitional cell populations cooperate with the microenvironment in untreated and chemo-resistant pancreatic cancer. Nat Genet 54:1390–1405
17. Ravi VM, Neidert N, Will P et al (2022) T-cell dysfunction in the glioblastoma microenvironment is mediated by myeloid cells releasing interleukin-10. Nat Commun 13:925
18. Wu SZ, Al-Eryani G, Roden DL et al (2021) A single-cell and spatially resolved atlas of human breast cancers. Nat Genet 53:1334–1347
19. Meylan M, Petitprez F, Becht E et al (2022) Tertiary lymphoid structures generate and propagate anti-tumor antibody-producing plasma cells in renal cell cancer. Immunity 55:527–541e525
20. (2014) Comprehensive molecular characterization of gastric adenocarcinoma. Nature 513:202–209

21. Cristescu R, Lee J, Nebozhyn M et al (2015) Molecular analysis of gastric cancer identifies subtypes associated with distinct clinical outcomes. Nat Med 21:449–456
22. Won Y, Choi E (2022) Mouse models of Kras activation in gastric cancer. Exp Mol Med 54:1793–1798
23. Till JE, Yoon C, Kim BJ et al (2017) Oncogenic KRAS and p53 loss drive gastric tumorigenesis in mice that can be attenuated by E-Cadherin expression. Cancer Res 77:5349–5359
24. Yamasaki J, Hirata Y, Otsuki Y et al (2022) MEK Inhibition suppresses metastatic progression of KRAS-mutated gastric cancer. Cancer Sci 113:916–925
25. Fu XH, Chen ZT, Wang WH et al (2019) KRAS G12V mutation is an adverse prognostic factor of Chinese gastric cancer patients. J Cancer 10:821–828
26. Lee SH, Lee D, Choi J et al (2025) Spatial dissection of tumour microenvironments in gastric cancers reveals the immunosuppressive crosstalk between CCL2+fibroblasts and STAT3-activated macrophages. Gut 74:714–727
27. Oh SC, Sohn BH, Cheong JH et al (2018) Clinical and genomic landscape of gastric cancer with a mesenchymal phenotype. Nat Commun 9:1777
28. Ooi CH, Ivanova T, Wu J et al (2009) Oncogenic pathway combinations predict clinical prognosis in gastric cancer. PLoS Genet 5:e1000676
29. Jiang H, Yu D, Yang P et al (2022) Revealing the transcriptional heterogeneity of organ-specific metastasis in human gastric cancer using single-cell RNA sequencing. Clin Transl Med 12:e730
30. Browaeys R, Saelens W, Saeys Y (2020) NicheNet: modeling intercellular communication by linking ligands to target genes. Nat Methods 17:159–162
31. Cable DM, Murray E, Shanmugam V et al (2022) Cell type-specific inference of differential expression in Spatial transcriptomics. Nat Methods 19:1076–1087
32. Zheng Y, Carrillo-Perez F, Pizurica M, Heiland DH, Gevaert O (2023) Spatial cellular architecture predicts prognosis in glioblastoma. Nat Commun 14:4122
33. Tanevski J, Flores ROR, Gabor A, Schapiro D, Saez-Rodriguez J (2022) Explainable multiview framework for dissecting Spatial relationships from highly multiplexed data. Genome Biol 23:97
34. Elosua-Bayes M, Nieto P, Mereu E, Gut I, Heyn H (2021) SPOTlight: seeded NMF regression to deconvolute Spatial transcriptomics spots with single-cell transcriptomes. Nucleic Acids Res 49:e50
35. Qiu X, Mao Q, Tang Y et al (2017) Reversed graph embedding resolves complex single-cell trajectories. Nat Methods 14:979–982
36. Pham D, Tan X, Balderson B et al (2023) Robust mapping of Spatiotemporal trajectories and cell-cell interactions in healthy and diseased tissues. Nat Commun 14:7739
37. Cang Z, Zhao Y, Almet AA et al (2023) Screening cell-cell communication in Spatial transcriptomics via collective optimal transport. Nat Methods 20:218–228
38. Jin S, Guerrero-Juarez CF, Zhang L et al (2021) Inference and analysis of cell-cell communication using cellchat. Nat Commun 12:1088
39. Van de Sande B, Flerin C, Davie K et al (2020) A scalable SCENIC workflow for single-cell gene regulatory network analysis. Nat Protoc 15:2247–2276
40. Hanzelmann S, Castelo R, Guinney J (2013) GSVA: gene set variation analysis for microarray and RNA-seq data. BMC Bioinformatics 14:7
41. Yu G, Wang LG, Han Y, He QY (2012) ClusterProfiler: an R package for comparing biological themes among gene clusters. OMICS 16:284–287
42. Yoshihara K, Shahmoradgoli M, Martinez E et al (2013) Inferring tumour purity and stromal and immune cell admixture from expression data. Nat Commun 4:2612
43. Becht E, Giraldo NA, Lacroix L et al (2016) Erratum to: estimating the population abundance of tissue-infiltrating immune and stromal cell populations using gene expression. Genome Biol 17:249
44. Mo S, Jin B, Tseng Y et al (2023) A precise molecular subtyping of ulcerative colitis reveals the immune heterogeneity and predicts clinical drug responses. J Transl Med 21:466
45. Tseng Y, Mo S, Zeng Y et al (2022) Machine Learning Model in Predicting Sarcopenia in Crohn's Disease Based on Simple Clinical and Anthropometric Measures. Int J Environ Res Public Health 20
46. Geeleher P, Cox N, Huang RS (2014) pRRophetic: an R package for prediction of clinical chemotherapeutic response from tumor gene expression levels. PLoS ONE 9:e107468
47. Jiang P, Gu S, Pan D et al (2018) Signatures of T cell dysfunction and exclusion predict cancer immunotherapy response. Nat Med 24:1550–1558
48. Qi Y, Hu Y, Lin C, Song G, Shi L, Zhu H (2025) A preoperative predictive model based on multi-modal features to predict pathological complete response after neoadjuvant chemoimmunotherapy in esophageal cancer patients. Front Immunol 16:1530279
49. Mayakonda A, Lin DC, Assenov Y, Plass C, Koeffler HP (2018) Maftools: efficient and comprehensive analysis of somatic variants in cancer. Genome Res 28:1747–1756
50. Maia A, Schöllhorn A, Schuhmacher J, Gouttefangeas C (2023) CAF-immune cell crosstalk and its impact in immunotherapy. Semin Immunopathol 45:203–214
51. Mao X, Xu J, Wang W et al (2021) Crosstalk between cancer-associated fibroblasts and immune cells in the tumor microenvironment: new findings and future perspectives. Mol Cancer 20:131
52. Lei ZN, Teng QX, Tian Q et al (2022) Signaling pathways and therapeutic interventions in gastric cancer. Signal Transduct Target Ther 7:358
53. Luo H, Xia X, Huang LB et al (2022) Pan-cancer single-cell analysis reveals the heterogeneity and plasticity of cancer-associated fibroblasts in the tumor microenvironment. Nat Commun 13:6619
54. Kang B, Camps J, Fan B et al (2022) Parallel single-cell and bulk transcriptome analyses reveal key features of the gastric tumor microenvironment. Genome Biol 23:265
55. Qi J, Sun H, Zhang Y et al (2022) Single-cell and Spatial analysis reveal interaction of FAP(+) fibroblasts and SPP1(+) macrophages in colorectal cancer. Nat Commun 13:1742
56. Wang R, Song S, Qin J et al (2023) Evolution of immune and stromal cell States and ecotypes during gastric adenocarcinoma progression. Cancer Cell 41:1407–1426e1409
57. Christian JI, Pastula A, Herbst A et al (2022) Loss of DRO1/CCDC80 in the tumor microenvironment promotes carcinogenesis. Oncotarget 13:615–627
58. Ferraro A, Schepis F, Leone V et al (2013) Tumor suppressor role of the CL2/DRO1/CCDC80 gene in thyroid carcinogenesis. J Clin Endocrinol Metab 98:2834–2843
59. Hong E, Park S, Ooshima A et al (2020) Inhibition of TGF-beta signalling in combination with nal-IRI plus 5-Fluorouracil/Leucovorin suppresses invasion and prolongs survival in pancreatic tumour mouse models. Sci Rep 10:2935
60. Wang WD, Wu GY, Bai KH et al (2020) A prognostic stemness biomarker CCDC80 reveals acquired drug resistance and immune infiltration in colorectal cancer. Clin Transl Med 10:e225
61. Huang C, Zhou Y, Feng X, Wang J, Li Y, Yao X (2023) Delivery of engineered primary Tumor-Derived exosomes effectively

suppressed the colorectal cancer chemoresistance and liver metastasis. ACS Nano 17:10313–10326
62. Teicher BA, Fricker SP (2010) CXCL12 (SDF-1)/CXCR4 pathway in cancer. Clin Cancer Res 16:2927–2931
63. Shakir M, Tang D, Zeh HJ et al (2015) The chemokine receptors CXCR4/CXCR7 and their primary heterodimeric ligands CXCL12 and CXCL12/high mobility group box 1 in pancreatic cancer growth and development: finding flow. Pancreas 44:528–534
64. Loetscher M, Geiser T, O'Reilly T, Zwahlen R, Baggiolini M, Moser B (1994) Cloning of a human seven-transmembrane domain receptor, LESTR, that is highly expressed in leukocytes. J Biol Chem 269:232–237
65. Sun X, Cheng G, Hao M et al (2010) CXCL12 / CXCR4 / CXCR7 chemokine axis and cancer progression. Cancer Metastasis Rev 29:709–722
66. Cane S, Ponnappan S, Ponnappan U (2012) Altered regulation of CXCR4 expression during aging contributes to increased CXCL12-dependent chemotactic migration of CD4(+) T cells. Aging Cell 11:651–658
67. Daniel SK, Seo YD, Pillarisetty VG (2020) The CXCL12-CXCR4/CXCR7 axis as a mechanism of immune resistance in Gastrointestinal malignancies. Semin Cancer Biol 65:176–188
68. Xue LJ, Mao XB, Ren LL, Chu XY (2017) Inhibition of CXCL12/CXCR4 axis as a potential targeted therapy of advanced gastric carcinoma. Cancer Med 6:1424–1436
69. Terai S, Fushida S, Tsukada T et al (2015) Bone marrow derived fibrocytes contribute to tumor proliferation and fibrosis in gastric cancer. Gastric Cancer 18:306–313
70. Izumi D, Ishimoto T, Miyake K et al (2016) CXCL12/CXCR4 activation by cancer-associated fibroblasts promotes integrin beta1 clustering and invasiveness in gastric cancer. Int J Cancer 138:1207–1219
71. Zhuang Y, Peng LS, Zhao YL et al (2012) CD8(+) T cells that produce interleukin-17 regulate myeloid-derived suppressor cells and are associated with survival time of patients with gastric cancer. Gastroenterology 143:951–962e958
72. Pallett LJ, Swadling L, Diniz M et al (2023) Tissue CD14(+) CD8(+) T cells reprogrammed by myeloid cells and modulated by LPS. Nature 614:334–342
73. Goedhart M, Gessel S, van der Voort R et al (2019) CXCR4, but not CXCR3, drives CD8(+) T-cell entry into and migration through the murine bone marrow. Eur J Immunol 49:576–589
74. Zhao Y, Lei Y, Ning H et al (2023) PGF(2α) facilitates pathological retinal angiogenesis by modulating endothelial FOS-driven ELR(+) CXC chemokine expression. EMBO Mol Med 15:e16373
75. Zhang Y, Ling L, Murad R et al (2025) Macropinocytosis maintains CAF subtype identity under metabolic stress in pancreatic cancer. Cancer Cell
76. Zhang Z, Yu Y, Zhang Z et al (2023) Cancer-associated fibroblasts-derived CXCL12 enhances immune escape of bladder cancer through inhibiting P62-mediated autophagic degradation of PDL1. J Exp Clin Cancer Res 42:316
77. Cerezo-Wallis D, Contreras-Alcalde M, Troule K et al (2020) Midkine rewires the melanoma microenvironment toward a tolerogenic and immune-resistant state. Nat Med 26:1865–1877